

1 **Measurement Report: Cloud condensation nuclei (CCN)**  
2 **activity in the South China Sea from shipborne**  
3 **observations during summer and winter of 2021: seasonal**  
4 **variation and anthropogenic influence.**

5 Hengjia Ou<sup>1</sup>, Mingfu Cai<sup>2\*</sup>, Yongyun Zhang<sup>1</sup>, Xue Ni<sup>1</sup>, Baoling Liang<sup>3</sup>, Qibin Sun<sup>4,5</sup>,  
6 Shixin Mai<sup>1</sup>, Cuizhi Sun<sup>6</sup>, Shengzhen Zhou<sup>1</sup>, Haichao Wang<sup>1</sup>, Jiaren Sun<sup>2</sup>, Jun Zhao<sup>1\*</sup>

7 <sup>1</sup>School of Atmospheric Sciences, Guangdong Province Key Laboratory for Climate Change and Natural  
8 Disaster Studies, Southern Marine Science and Engineering Guangdong Laboratory (Zhuhai), Sun Yat-  
9 sen University, Zhuhai, Guangdong 519082, China

10 <sup>2</sup>Guangdong Province Engineering Laboratory for Air Pollution Control, Guangdong Provincial Key  
11 Laboratory of Water and Air Pollution Control, South China Institute of Environmental Sciences, MEE,  
12 Guangzhou 510655, China

13 <sup>3</sup>Guangzhou Sub-branch of Guangdong Ecological and Environmental Monitoring Center, Guangzhou  
14 510006, China

15 <sup>4</sup>Dongguan Meteorological Bureau, Dongguan, Guangdong, 523086, China

16 <sup>5</sup>Dongguan Engineering Technology Research Center of Urban Eco-Environmental Meteorology,  
17 Dongguan, Guangdong, 523086, China

18 <sup>6</sup>Southern Marine Science and Engineering Guangdong Laboratory (Zhuhai), Zhuhai, Guangdong  
19 519082, China

20  
21 *Correspondence:* Mingfu Cai (caimingfu@scies.org) and Jun Zhao (zhaojun23@mail.sysu.edu.cn)

22

**Style Definition:** Figure caption title: Indent:  
First line: 0 ch, Space Before: 0 pt, After: 0  
pt

23 **Abstract**

24 Understanding seasonal variations in cloud condensation nuclei (CCN) activity and the impact of  
25 anthropogenic emissions in marine environments is crucial for assessing climate change. This study  
26 presents findings from two shipborne observations conducted in the South China Sea (SCS) during the  
27 summer and winter of 2021. In summer, higher particle number concentrations but lower mass  
28 concentrations of non-refractory submicron particles (NR-PM<sub>1</sub>) were observed, driven by Aitken mode  
29 particle dominance. In contrast, winter showed a more balanced distribution between Aitken and  
30 Accumulation mode particles. Summer particles were more hygroscopic, exhibiting higher activation  
31 ratios (ARs) at all supersaturation (SS) levels. Distinct air mass periods were identified: in summer,  
32 terrestrial air masses from Luzon ("Luzon" period), the Indochinese Peninsula ("Indochinese Peninsula"  
33 period), and marine air masses; in winter, periods were influenced by Mainland China ("Mainland China"  
34 period), a mix of Mainland China and marine air masses ("Mixed" period), and purely marine air masses.  
35 The "Luzon" period in summer exhibited the highest particle number concentration, especially in the  
36 Aitken mode, resulting in the highest CCN number concentration (N<sub>CCN</sub>). Aerosol hygroscopicity was  
37 higher during the "Indochinese Peninsula" period compared to the "Luzon" period, leading to a higher  
38 bulk AR due to the combination of higher hygroscopicity and a greater fraction of accumulation mode  
39 particles. The "Mainland China" period in winter showed a high nitrate fraction in the NR-PM<sub>1</sub>, but the  
40 inorganic fraction was similar to it in "Luzon" period, resulting in comparable hygroscopicity at low SS  
41 to the "Luzon" period. However, smaller particle hygroscopicity was significantly lower in the  
42 "Mainland China" period compared to summer. The "Mixed" period in winter exhibited a higher fraction  
43 of accumulation mode particles, causing a higher bulk AR compared to the "Mainland China" period.  
44 Overall, summer terrestrial air masses increased the Aitken mode particle and CCN concentration, while  
45 winter terrestrial air masses led to higher concentration of large particles and lower hygroscopicity of  
46 fine particles. CCN closure analysis, considering aerosol composition and mixing state, revealed that  
47 summer aerosols were primarily internally mixed, whereas smaller aerosols in winter were primarily  
48 externally mixed. The potential effect of undetected sea salt may lead to an underestimation of aerosol  
49 hygroscopicity in summer. This study highlights significant seasonal differences in aerosol properties  
50 and the impact of different types of terrestrial air masses on CCN activity in the SCS, contributing to our  
51 understanding of regional climate influences.

## 52 **1.Introduction**

53 Aerosols can act as cloud condensation nuclei (CCN), influencing cloud formation, lifespan, and  
54 albedo, thus indirectly impacting global radiative balance (Fletcher et al., 2011; Albrecht, 1989). The  
55 aerosol-cloud interaction currently represents the largest uncertainty in radiative forcing within climate  
56 models, ranging from -1.7 to -0.3 W m<sup>-2</sup> (IPCC, 2021). This uncertainty can be partially attributed to the  
57 significant spatiotemporal variability in the aerosol size distribution and the ability of atmospheric  
58 aerosol particles acting as CCN (CCN activity) (Fitzgerald, 1973; Jimenez et al., 2009; Sihto et al., 2011).  
59 Thus, field measurements of aerosol size distribution and physicochemical properties are needed to better  
60 understand the radiative forcing exerted by atmospheric aerosol particles.

61 Previous studies suggest that particle number size distribution (PNSD) is a primary factor  
62 influencing CCN concentrations (Dusek et al., 2006; Rose et al., 2010; Pöhlker et al., 2016; Burkart et  
63 al., 2011). The PNSD can account for 84–96% of the variability in the CCN concentrations ( $N_{CCN}$ ) (Dusek  
64 et al., 2006), while CCN activities may also play a significant role in the  $N_{CCN}$  (Quinn et al., 2008; Cai  
65 et al., 2018; Ovadnevaite et al., 2017; Liu et al., 2018; Crosbie et al., 2015), which are primarily governed  
66 by the particle size, chemical composition, mixing state, surface tension, and hygroscopicity (Köhler,  
67 1936; Seinfeld and Pandis, 2016). Among these factors, the impact of hygroscopicity on CCN activities  
68 has received great attention in recent years (Petters and Kreidenweis, 2007; Ajith et al., 2022; Rose et al.,  
69 2010). Petters and Kreidenweis (2007) proposed the  $\kappa$ - Köhler theory based on the Köhler theory to  
70 quantify the ability of aerosol particles to absorb moisture and become CCN based on the aerosol  
71 hygroscopicity parameters ( $\kappa$ ). Ajith et al. (2022) showed that 64% of particles can be activated as CCN  
72 when  $\kappa$  is equal to 0.37, whereas when  $\kappa$  decreases to 0.23, only 48% of particles can be activated in the  
73 tropical coastal area.

74 Significant seasonal variations in PNSD and hygroscopicity under both terrestrial and marine  
75 environments were observed in previous field observations, leading to the seasonal variations in  $N_{CCN}$   
76 (Crosbie et al., 2015; Schmale et al., 2018; Burkart et al., 2011; Bougiatioti et al., 2009; Sihto et al., 2011;  
77 Leena et al., 2016; Ross et al., 2003; Gras and Keywood, 2017; Quinn et al., 2019). Crosbie et al. (2015)  
78 revealed that in the urban area of Arizona particles had larger sizes, higher hygroscopicity, and  $N_{CCN}$  was  
79 also higher during winter, while a higher abundance of smaller particles was observed during summer  
80 owing to stronger photochemical reactions. In pristine environments like mountain, coastal, and forested

81 regions, seasonal variations in  $N_{CCN}$  and PNSD were more pronounced than urban and rural areas  
82 (Schmale et al., 2018). Pöhlker et al. (2016) observed significant differences in  $N_{CCN}$  between the wet  
83 and dry seasons in the Amazon rainforest, while the  $\kappa$  values remained relatively stable. They also noted  
84 increased particle concentrations and aerosol hygroscopicity, both subject to the impact of long-range  
85 transport originating from anthropogenic emissions. Observations in marine areas during different  
86 seasons are relatively scarce compared with those in inland areas. Gras (1995) found that both particle  
87 concentration and  $N_{CCN}$  in the Southern Ocean reached their peaks during summer and gradually decrease  
88 to their valleys in winter. Quinn et al. (2019) showed that sea spray aerosols make a relatively significant  
89 contribution to  $N_{CCN}$  only during winter in the Western North Atlantic, while in other seasons, the primary  
90 contribution comes from biogenic aerosols oxidized from dimethyl sulfide (DMS). Zheng et al. (2020)  
91 revealed that sulfate dominates the particle condensational growth to CCN sizes during summer in the  
92 Eastern North Atlantic, while secondary organic aerosols played a significant role in particle growth  
93 throughout all seasons. These results indicate that CCN activity and concentration could vary in a large  
94 range during different seasons. Thus, further observations across different seasons in marine  
95 environments are needed to enhance our understanding of marine CCN activities and their seasonal  
96 variations.

97 The South China Sea (SCS), located in Southeast Asia and bordered by China, the Indochinese  
98 Peninsula, and Maritime Southeast Asia, is significantly influenced by air pollutants transported through  
99 terrestrial air masses. Studies have shown that these pollutants play a crucial role in determining aerosol  
100 concentration and properties in the region (Atwood et al., 2017; Xiao et al., 2017; Geng et al., 2019;  
101 Liang et al., 2021; Sun et al., 2023; Qin et al., 2024). For instance, Xiao et al. (2017) reported that 69.7%  
102 of nitrate and 57.5% of sulfate in the SCS originated from fossil fuel combustion, particularly coal  
103 burning in Chinese coastal regions. Additionally, Liang et al. (2021) and Sun et al. (2023) observed an  
104 increase in the organic fraction and concentration of submicron aerosols when the region was influenced  
105 by terrestrial air masses from Mainland China and the Indochinese Peninsula in the northern SCS. Further  
106 studies highlighted the variation in aerosol properties under different air mass influences. Atwood et al.  
107 (2017) found a significant bimodal particle distribution with a  $\kappa$  value of 0.65 in the southern SCS under  
108 marine air mass influence, whereas a unimodal distribution with a  $\kappa$  of 0.4 was observed under  
109 continental air mass influence.

110 The SCS experiences a typical monsoon climate with distinct seasonal wind direction changes  
111 (Wang et al., 2009). The northeast monsoon, occurring from November to March, is characterized by  
112 stronger average wind speeds and longer period compared to the southwest monsoon, which dominates  
113 from June to August. The transitional periods occur from April to May and September to October. During  
114 the northeast monsoon, air pollutants are primarily transported to the SCS by terrestrial air masses from  
115 China (Xiao et al., 2017; Liu et al., 2014; Geng et al., 2019). In contrast, during the summer, pollutants  
116 mainly originate from terrestrial air masses from the Indochinese Peninsula and Maritime Southeast Asia  
117 (Geng et al., 2019; Liang et al., 2021; Sun et al., 2023). These varying sources of anthropogenic emissions  
118 exert different impacts on CCN activity differently across seasons. Additionally, when the marine  
119 boundary layer over the SCS is influenced by various natural and anthropogenic sources, resulting in  
120 altered aerosol properties, the characteristics of cumulus clouds are correspondingly affected (Miller et  
121 al., 2023). This indicates that aerosol-cloud interactions vary between winter and summer seasons.  
122 However, due to limited observational data, our understanding of seasonal variations in CCN activity in  
123 the SCS remains incomplete. Conducting comprehensive observational studies on CCN activity across  
124 different seasons is essential for improving our understanding of aerosol-cloud interactions on the SCS.

125 In this study, we conducted two shipborne observations in the SCS during summer (May 5–June 9,  
126 2021) and winter (December 19–29, 2021). Our observations with online instruments focused on  
127 measuring aerosol chemical composition, PNSD, and CCN activation in the region. Our results provide  
128 valuable insights into the differences in CCN activity between winter and summer, as well as the  
129 influence of different types of terrestrial air masses on CCN activity in the SCS across different seasons.

## 130 **2. Methodology**

### 131 **2.1 Cruise information and onboard measurements**

#### 132 **2.1.1 Cruise information**

133 This study consists of two research cruises conducted during the summer and winter of 2021,  
134 respectively. These two cruises were interdisciplinary scientific expeditions, integrating fields such as  
135 marine geology, oceanography, and atmospheric environment. The primary objective in atmospheric  
136 environment was to investigate the impact of summer and winter monsoons on the atmospheric  
137 environment of the South China Sea (SCS). The summer and winter cruises were carried out respectively  
138 by the vessels "Tan Kah Kee" and "Sun Yat-sen University". The "Tan Kah Kee" is an oceanographic

139 research vessel with a length of 77.7 meters, a beam of 16.24 meters, and a displacement of 3611 tons.  
140 The "Sun Yat-sen University" is a comprehensive oceanographic training vessel with a total length of  
141 114.3 meters, a beam of 19.4 meters, and a displacement of 6880 tons.

142 The first cruise was from May 5<sup>th</sup> to June 9<sup>th</sup>, 2021. The cruise started from Xiamen Port and  
143 traversed from the northern to the central-southern South China Sea, and then circled back near Hainan  
144 Island, and finally returned to Xiamen Port. The second cruise was from December 19<sup>th</sup> to December  
145 29<sup>th</sup>, 2021. It began from Gaolan Port in Zhuhai and reached the vicinity of Yongxing Island, and  
146 ultimately returned to Gaolan Port (Fig. 1a). Unfortunately, due to adverse weather conditions, such as  
147 strong winter monsoon winds causing poor sea conditions, and the fact that it was the first scientific  
148 deployment of the research vessel Sun Yat-sen University, the winter cruise had a shorter duration and  
149 covered a narrower spatial range, remaining only in the northern SCS (Fig. S1), compared to the summer  
150 cruise. On both cruises, most of the instruments were housed in a single compartment and the sampling  
151 lines were extended from the window of the compartment to the height of the ship's bridge (~17 m above  
152 sea level) (Fig. 1a).

### 153 2.1.2 Size-resolved cloud condensation nuclei activity measurement

154 The size-resolved CCN activity was measured using the scanning mobility CCN analysis (SMCA)  
155 method proposed by Moore et al. (2010), employing a combination of a scanning mobility particle sizer  
156 (SMPS) system and a cloud condensation nuclei counter (CCNc-200, DMT Inc., USA) (Fig. S2). The  
157 SMPS system consisted of a differential mobility analyzer (DMA; model 3082, TSI, Inc.) and a  
158 condensation particle counter (CPC; model 3756, TSI Inc.). The SMPS and the CCNc system were used  
159 to measure PNSD and size-resolved CCN number concentration at a mobility size range of 10–500 nm  
160 and 10–593 nm in summer and winter campaign, respectively. Unfortunately, due to the malfunction of  
161 flow sensor in the column B on both cruises, only the data from column A is presented in this study.  
162 During the SMCA measurement, the particles were first passed through a Nafion dryer to remove  
163 moisture, then neutralized using a neutralizer. After that, they were subjected to size selection with a  
164 DMA. The particles were then split between a CPC (1 L min<sup>-1</sup>) for particle concentration measurement  
165 and a CCNc (0.5 L min<sup>-1</sup>) for CCN measurement at a specific supersaturation (SS). To maintain sample  
166 flow through the DMA, dilution air (0.5 L min<sup>-1</sup>) was added to the CPC inlet stream. The effect of the  
167 dilution air was accounted for in the PNSD data processing (Fig. S2). The supersaturation of the CCNc

168 was set at 0.2 %, 0.4 %, and 0.7 % in summer campaign and 0.1%, 0.2 %, 0.4 %, and 0.7 % in winter  
169 campaign, respectively. During the measurement process, each supersaturation level was held constant  
170 for 20 minutes, with the DMA completing a full scanning cycle every 5 minutes. During the  
171 measurements, supersaturation levels varied incrementally between 0.1% and 0.2%, 0.2% and 0.4%, and  
172 0.4% and 0.7%, with temperature stabilization times ranging from a few seconds to several tens of  
173 seconds. However, reducing the supersaturation from 0.7% to 0.1% or 0.2% required approximately 5  
174 minutes for stabilization. For data processing, only instances where the temperature remained stable  
175 throughout the DMA scanning phase were included in the analysis. Before the measurements, the CCNc  
176 was calibrated with ammonium sulfate ((NH<sub>4</sub>)<sub>2</sub>SO<sub>4</sub>) particles at each set SS. Detailed description of the  
177 instrument configuration and calibration can be found in Cai et al. (2018). The uncertainty in the  
178 instrument's measurement of size-resolved particle number concentration is approximately 5%-6%  
179 (Morre et al. 2010).

### 180 **2.1.3 Aerosol chemical composition measurement**

181 The chemical composition of atmospheric non-refractory submicron particulate matter (NR-PM<sub>1</sub>),  
182 including sulfate, nitrate, organics, ammonium, and chloride, was measured using an online time-of-  
183 flight ACSM (ToF-ACSM; Aerodyne Inc., USA). The sampling time of the ToF-ACSM was  
184 approximately 10 min. The ionization efficiency (IE) and relative ionization efficiency (RIE) values of  
185 the instrument were calibrated using ammonium nitrate (NH<sub>4</sub>NO<sub>3</sub>) and ammonium sulfate ((NH<sub>4</sub>)<sub>2</sub>SO<sub>4</sub>)  
186 both before the start and after the completion of the campaigns. The calibration gives an IE value of  
187 103.4 ions pg<sup>-1</sup> and 98.9 ions pg<sup>-1</sup> for nitrate in summer and winter cruises, respectively. The RIE values  
188 for ammonium were 3.31 and 3.33 during the summer and winter, respectively, while the ones for sulfate  
189 were 1.02 and 0.81 during the summer and winter, respectively. The collection efficiency (CE) was  
190 determined as shown in Sun et al. (2023) and time-independent CE values were used in this study.  
191 Detailed CE calculation and discussion can be found in the supplementary (Text S1, and Fig. S3). The  
192 values obtained using the time-independent CE method show a deviation of approximately 3% compared  
193 to those obtained with a constant CE of 0.5. Assuming an average aerosol density of 1.5 g cm<sup>-3</sup> (Geller  
194 et al., 2006), the mass concentrations measured by the SMPS and ToF-ACSM exhibit a strong overall  
195 correlation, with correlation coefficients of 0.84 in summer and 0.93 in winter. During the pre-onset  
196 phase of the summer monsoon (prior to May 24), periodic discrepancies were observed between the

197 ACSM and SMPS data, likely due to the influence of refractory aerosol (ie. Black carbon). This issue is  
198 discussed in detail in Text S1. The black carbon (BC) mass concentrations were measured using an  
199 aethalometer (Model AE33, Magee Scientific, USA) with a 1-minute time resolution (Drinovec et al.,  
200 2015). Notably, the BC mass concentrations obtained from AE33 are referred to as equivalent BC mass  
201 concentrations, as they represent the combined light absorption of BC at 880 nm. Prior to entering the  
202 AE33, the sampled air was passed through a PM<sub>2.5</sub> cyclone (BGI Inc., Waltham, MA, USA) to exclude  
203 particles larger than 2.5 μm.

#### 204 2.1.4 Meteorological parameter measurements

205 The meteorological elements, including temperature, relative humidity (RH), wind speed, and wind  
206 direction, were measured by the combined automatic weather station (AWS430, Vaisala Inc., Finland)  
207 onboard the vessels (Sun et al., 2024). During the winter cruises, meteorology data before 12.22 was  
208 missed due to the calibration for the automatic weather station (WXT536, Vaisala Inc., Finland) before  
209 12.22. The timeseries of meteorological data were presented in Fig. S5. The AWS430 provides  
210 measurement accuracies of ±2% for wind speed, ±2% for wind direction, ±0.3°C for temperature, and  
211 ±1% for relative humidity (within the range of 0–90%). Similarly, the WXT536 offers accuracies of ±3%  
212 for wind speed, ±3% for wind direction, ±0.3°C for temperature, and ±3% for relative humidity (within  
213 the range of 0–90%) (www.vaisala.com).

## 214 2.2 Data analysis

### 215 2.2.1 CCN activation

216 The size-resolved number concentration of total particle and cloud condensation nuclei were  
217 obtained from the SMPS and CCNc through the SMCA method. The activation diameter was determined  
218 by fitting the activation ratio (AR,  $N_{CCN}/N_{CN}$ ) and dry diameter at each supersaturation through the  
219 following equation:

$$220 \quad AR = \frac{B}{1 + \left(\frac{D_P}{D_{50}}\right)^C}, \quad (1)$$

221 where AR indicates the size-resolved AR,  $D_P$  represents dry particle diameter (nm); B, C, and  $D_{50}$  are the  
222 three fitting parameters, representing the asymptote, the slope, and the inflection point of the sigmoid,  
223 respectively (Moore et al., 2010). The  $D_{50}$  parameter, also known as the critical diameter, corresponds to



224 the particle size at which 50% of the particles are activated at a specific SS. The fitting results from  
225 SMCA method measured in this study are presented in Fig. S6.

226 The hygroscopicity parameter ( $\kappa$ ) which represents CCN activity according to  $\kappa$ -Köhler equation is  
227 calculated as follows (Petters and Kreidenweis, 2007):

$$228 \quad \kappa = \frac{4A^3}{27D_{50}^3(\ln S_c)^2}, \quad A = \frac{4\sigma_{s/a}M_w}{RT\rho_w} \quad (2)$$

229 where  $\rho_w$  is the density of pure water (about  $997.04 \text{ kg m}^{-3}$  at  $298.15 \text{ K}$ ),  $M_w$  is the molecular weight of  
230 water ( $0.018 \text{ kg mol}^{-1}$ ),  $\sigma_{s/a}$  corresponds to the surface tension of the solution-air interface and is assumed  
231 to be equal to the surface tension of pure water ( $\sigma_{s/a}=0.0728 \text{ N m}^{-1}$  at  $298.15 \text{ K}$ ),  $R$  is the universal gas  
232 constant ( $8.314 \text{ J mol}^{-1} \text{ K}^{-1}$ ),  $T$  denotes thermodynamic temperature in kelvin ( $298.15 \text{ K}$ ), and  $D_{50}$  is the  
233 critical diameter (in m). Additionally, it is noting that the estimated  $\kappa$  values refer to particles with the  
234  $D_{50}$ .

235 According to  $\kappa$ -Köhler theory, in the following discussion, the hygroscopicity of small particles is  
236 associated with hygroscopicity at high SS, whereas the hygroscopicity of large particles is linked to  
237 hygroscopicity at low SS.

238 During part of the summer measurement period, the  $D_{50}$  at 0.7% supersaturation ranged between 30  
239 and 40. However, due to lower concentrations during these times, instrument noise introduced greater  
240 measurement uncertainty, as demonstrated in Fig. S7. Consequently, the average  $D_{50}$  and  $\kappa$  at 0.7% SS  
241 are not included in Table 1.

### 242 2.2.2 Closure Method

243 According to Petters and Kreidenweis. (2007),  $\kappa$  can be predicted by a simple mixing rule based on  
244 chemical volume fractions:

$$245 \quad \kappa_{sim} = \sum_i \varepsilon_i \kappa_i \quad (3)$$

246 where  $\varepsilon_i$  and  $\kappa_i$  are the volume fraction and hygroscopicity parameter for the specific dry component  
247 in the mixture. We obtained  $\varepsilon$  from aerosol chemical composition measured by the ToF-ACSM. In this  
248 study,  $\kappa$  for  $(\text{NH}_4)_2\text{SO}_4$  (0.48),  $\text{NH}_4\text{NO}_3$  (0.58), and  $\text{NaCl}$  (1.1) represent the  $\kappa$  of  $\text{SO}_4^{2-}$ ,  $\text{NO}_3^-$ , and  $\text{Cl}^-$   
249 provided by the ToF-ACSM (Huang et al., 2022). Besides, the  $\kappa$  of organic was 0.1 at this study according  
250 to Huang et al. (2022). The density of  $(\text{NH}_4)_2\text{SO}_4$ ,  $\text{NH}_4\text{NO}_3$ ,  $\text{NaCl}$  and organic are  $1769 \text{ kg m}^{-3}$ ,  $1720 \text{ kg}$   
251  $\text{m}^{-3}$ ,  $2165 \text{ kg m}^{-3}$ , and  $1400 \text{ kg m}^{-3}$  (Huang et al., 2022; Gysel et al., 2007).

### 252 2.2.3 CCN concentration and activation ratio calculation

253 Due to the malfunction of the column B, the CCN concentration ( $N_{CCN}$ ) was calculated based on the  
254 size-resolved AR at a specific SS from SMCA method and observed particle number concentration. It  
255 can be calculated by the following equation (Cai et al., 2018):

$$256 N_{CCN}(SS) = \int_0^{\infty} AR(SS, D_p) N_{CN}(D_p) dD_p \quad (4)$$

257 where  $N_{CCN}(SS)$  is the CCN concentration at a specific SS,  $AR(SS, D_p)$  is the ratio of  $N_{CCN}$  at a specific  
258 SS to  $N_{CN}$  on a specific diameter from the SMCA method and  $N_{CN}(D_p)$  is the particle number  
259 concentration at a specific diameter ( $D_p$ ). Due to the absence of direct measurements for total  $N_{CCN}$ , we  
260 refer to the  $N_{CCN}$  derived from Eq. (4) as observed values ( $N_{CCN,obs}$ ) in this study. Previous research has  
261 shown that this method (size-resolved CCN from one column in CCNc-200) provides results closely  
262 matching those obtained from direct measurement (from another column in CCNc-200), supporting its  
263 reliability (Meng et al., 2014; Lathem and Nenes, 2011).

264 The  $N_{CCN}$  (referred as  $N_{CCN,sim}(SS)$ ) can be predicted by  $D_{50}$  from closure method ( $D_{50,sim}(SS)$ )  
265 and  $N_{CN}$  according to following equation (Jurányi et al., 2011):

$$266 N_{CCN,sim}(SS) = \int_{D_{50,sim}(SS)}^{\infty} N_{CN}(D_p) dD_p \quad (5)$$

267 where the  $D_{50,sim}(SS)$  is calculated based on the eq. (2) and (3).

268 The bulk AR at a specific SS can be calculated by:

$$269 AR(SS) = \frac{N_{CCN,obs}(SS)}{N_{CN,tot}} \quad (6)$$

270 where the  $N_{CN,tot}$  represents the total particle number concentration.

271 To investigate the impact of the fraction and mixing state of aerosol on  $N_{CCN}$ , two CCN simulation  
272 schemes are applied in this study (Patel et al., 2021).

273 (1) Internal-mixed scheme: the aerosol composition from the ToF-ACSM was assumed to be size-  
274 independent and internally mixed. All aerosols have an identical chemical composition in the  
275 whole size range.  $N_{CCN}$  is calculated by  $\kappa_{sim}$  and measured PNSD according to Eq. (2), Eq. (3),  
276 and Eq. (5) (Fig. S8a).

277 (2) External-mixed scheme: the aerosol composition from the ToF-ACSM was assumed to be size-  
278 independent and externally mixed. Four types of aerosols ( $(NH_4)_2SO_4$ ,  $NH_4NO_3$ , NaCl and  
279 organic) are assumed to have the same proportion for all sizes. The  $D_{50}$  from each species was

280 calculated by Eq. (2) according to their  $\kappa$  values mentioned in 2.2.2.  $N_{CCN}$  is calculated  
 281 according to the Eq. (5) (Fig. S8b and Table S1).

282 To access the simulation result from these two schemes, normalized mean bias (NMB) was used in  
 283 this study:

$$284 \quad NMB = \frac{\sum(N_{CCN,sim} - N_{CCN,obs})}{\sum N_{CCN,obs}} \quad (7)$$

285 where  $N_{CCN,sim}$  is the simulated  $N_{CCN}$  from two schemes, and  $N_{CCN,obs}$  is the observed  $N_{CCN}$ .

#### 286 2.2.4 Fitting of log-normal modes to particle number size distributions

287 The multi-lognormal distribution function (Eq. (8)) is used to parameterize and optimize the  
 288 descriptions of the measured PNSD (Heintzenberg, 1994) and is widely applied in aerosol research (Cai  
 289 et al., 2020; Boyer et al., 2023; Zhu and Wang, 2024). An automatic mode-fitting algorithm (Hussein et  
 290 al., 2005) is used to generate the model-fitted results.

$$291 \quad f(D_p, \bar{D}_{pg,i}, N_i, \sigma_{g,i}) = \sum_{i=1}^n \frac{N_i}{\sqrt{2\pi \log(\sigma_{g,i})}} \times \exp \left[ -\frac{[\log D_p - \log \bar{D}_{pg,i}]^2}{2(\log \sigma_{g,i})^2} \right] \quad (8)$$

292 where  $D_p$  is the diameter of a particle. Each lognormal mode is characterized by three parameters:  
 293 the mode number concentration ( $N_i$ ), geometric variance ( $\sigma_{g,i}$ ), and geometric mean diameter (GMD,  
 294  $\bar{D}_{pg,i}$ ). The total number of lognormal modes used to describe the PNSD is denoted by  $n$ . These modes  
 295 are fitted using an algorithm applied to each particle size distribution, with one to three log-normal  
 296 distributions used per time step. The algorithm classifies the PNSD into nucleation, Aitken, and  
 297 accumulation modes based on their geometric mean diameters (GMDs). The GMD for nucleation modes  
 298 (GMD1) typically ranges from 3 to 30 nm, for Aitken modes (GMD2) from 30 to 100 nm, and for  
 299 accumulation modes (GMD3) above 100 nm (Heintzenberg, 1994; Hussein et al., 2005; Zhu and Wang,  
 300 2024).

#### 301 2.2.5 Backward trajectory simulation and cluster analysis

302 Backward trajectory calculations were performed using the MeteoInfo, an open-source software  
 303 (Wang, 2014) to determine potential source origins. Weekly GDAS1 (Global Data Assimilation System  
 304 at a resolution of 1°) files were downloaded from the NOAA Air Resource Laboratory (ARL) website  
 305 (<https://www.ready.noaa.gov/gdas1.php>). The calculation of backward trajectories is performed every  
 306 1 hour based on the location mentioned below, generating 72-hour backward trajectories at 500m.

307 To clarify the sources of air masses, the cluster analysis was applied in this study, which was  
308 performed by TrajStat, a plug-in module of MeteoInfo, based on k-means method  
309 ([http://meteothink.org/docs/trajstat/cluster\\_cal.html](http://meteothink.org/docs/trajstat/cluster_cal.html)). According to the report by the China  
310 Meteorological Administration (Chao et al., 2022), the summer monsoon in 2021 broke out during the  
311 sixth pentad of May. Therefore, based on the timing of the monsoon onset and the actual trajectory of the  
312 ship, we selected two representative midpoints of the ship track for backward trajectory calculations and  
313 cluster analysis in summer: the midpoint of the ship's track before the onset of the summer monsoon  
314 (May 5-23) and the midpoint of the track after the summer monsoon began (May 24-June 9). In the  
315 winter cruise, backward trajectories calculation and cluster analysis were performed at two specific  
316 locations: the ship's anchorage near Big Ten-thousand Mountain Island (December 19-22 and December  
317 27-29) and the midpoint between Dawan Mountain Island and Yongxing Island (December 23-26). To  
318 ensure the accuracy of the backward trajectory calculations and cluster analysis, we compared the  
319 trajectories at the midpoints with those from the ship's actual locations to verify consistency in air mass  
320 sources (Fig. S9). Minor discrepancies may exist between the air mass origins at certain midpoints and  
321 the actual ship locations. However, overall, the air mass origins at the midpoints are representative of  
322 those at the actual locations. We further examined the trajectories for each cluster to verify their alignment  
323 with the air mass origins they represent (Fig. S10). The results demonstrate that cluster analysis was well  
324 conducted. Additionally, figure S10 illustrates the average altitude variation as the age in hours increases  
325 across different periods. During summer, the altitude of the clusters remained below 880 hPa, indicating  
326 that they resided within the boundary layer (about 800 hPa). While in winter, the altitude of the clusters  
327 was higher than in summer, especially for the cluster during the mixed period (peaked at about 755 hPa).  
328 However, these clusters were generally within or close to the boundary layer. These results suggest that  
329 the back trajectories could represent the characteristics of the air masses originating from these specified  
330 regions.

### 331 2.2.5 Data quality control

332 To ensure reliable atmospheric samples in the SCS and mitigate the influence of research vessel  
333 emissions, we applied the following data processing procedures (Huang et al., 2018; Cai et al., 2020;  
334 Liang et al., 2021).

335 Firstly, we identified organic compounds, black carbon (BC), and small particulate matter (41.4 nm  
336 particles) as indicators of ship emissions, recognizing their sudden peak values as indicative of the ship's  
337 own emissions.

338 Secondly, we accounted for the relative positions of the ship's chimney and the sampling tube.  
339 During the summer cruise, we excluded data corresponding to a relative wind direction (with respect to  
340 the ship's bow) between 150° and 270° and a relative wind speed (with respect to the ship's speed) of less  
341 than 2.5 m s<sup>-1</sup> (Fig. S12a, Fig. S13a1, and Fig. S14a-c). During the winter cruise, we excluded data for a  
342 relative wind direction between 150° and 220° and a relative wind speed of less than 2.5 m s<sup>-1</sup> (Fig. S12b,  
343 Fig. S13b1, and Figs. S14d-f).

344 Applying these criteria, 74.8% of the data in summer and 92.2% in winter (both at 10-minute  
345 resolution) were classified as “clean” and retained for analysis. The timeseries of data before and after  
346 quality control is shown in Fig. S15.

### 347 **3. Results and discussion**

#### 348 **3.1 CCN concentration and aerosol characteristics over SCS in summer and winter**

349 Figure 2 presented the timeseries of PNSD (a1 and a2), NR-PM<sub>1</sub> mass concentrations and fractions  
350 (b1 and b2, c1 and c2), number concentrations of CCN (d1 and d2), and hygroscopicity  $\kappa$ -values (e1 and  
351 e2) during two campaigns in summer and winter. During the summer cruise, we observed two distinct  
352 periods around the onset of the summer monsoon. The South China Sea (SCS) summer monsoon began  
353 in the sixth pentad of May (Chao et al., 2022). In winter, the influence of the winter monsoon persisted  
354 throughout the entire observation period (Fig. 1c). Despite our measurements being limited to the  
355 northern SCS in winter, the impact of the Northeast Monsoon on the SCS was evident.

356 The average particle number concentration in summer (6966 cm<sup>-3</sup>) was higher than in winter (4988  
357 cm<sup>-3</sup>), primarily due to the higher number concentration of Aitken-mode particles in summer (Fig. 3a-b).  
358 In summer, particles were concentrated in smaller sizes, whereas in winter, particle size distribution was  
359 relatively balanced between the Aitken mode (2185 cm<sup>-3</sup>) and the accumulation mode (2176 cm<sup>-3</sup>) (Fig.  
360 3a-b).

361 The average mass concentration of NR-PM<sub>1</sub> was 3.76  $\mu\text{g m}^{-3}$  in summer and increased to 9.39  $\mu\text{g}$   
362  $\text{m}^{-3}$  in winter (Fig. 3c-d). In summer, the dominant aerosol component was sulfate (45.5%), followed by  
363 organics (35.8%), ammonium (12.9%), nitrate (4.0%), and chloride (1.9%) (Fig. 3c), similar to the

364 pattern observed in the northern SCS during the summer of 2018 (Fig. 3e) (Liang et al., 2021). However,  
365 in winter, organics became the predominant aerosol component (37%), with nitrate (22.2%) replacing  
366 sulfate (18.9%) as the highest proportion of inorganic components (Fig. 3d). Although  $N_{CN}$  was higher  
367 in summer than in winter, the particle volume size distribution indicates that a higher fraction of particles  
368 was concentrated in larger size in winter, which significantly influenced mass concentration, resulting in  
369 a higher NR-PM<sub>1</sub> concentration (Fig. S16).

370 The average number concentration of cloud condensation nuclei ( $N_{CCN}$ ) in summer was higher than  
371 in winter at all supersaturation (SS) levels (Table 1). The ratio of  $N_{CCN}$  between summer and winter was  
372 smaller at high SS ( $N_{CCN, winter}/N_{CCN, summer} = 0.51$  and  $0.54$  at  $0.4\%$  SS and  $0.7\%$  SS, respectively)  
373 compared to low SS ( $N_{CCN, winter}/N_{CCN, summer} = 0.62$  at  $0.2\%$  SS), likely due to the significant difference in  
374 number concentration of Aitken-mode particles between the two seasons (Fig. 3a-b). Compared to the  
375 observation in the Yellow Sea, a region similarly influenced by terrestrial air masses from mainland  
376 China, the  $N_{CCN}$  were lower in winter, while in summer, the  $N_{CCN}$  were more comparable to those  
377 observed in the Yellow Sea ( $4821 \text{ cm}^{-3}$  at  $0.63\%$  SS) (Park et al., 2018).

378 The aerosol hygroscopicity ( $\kappa$ ) was higher in summer than that in winter (Table 1). Besides, the  
379 hygroscopicity pattern varied between seasons: in summer,  $\kappa$  increased with SS (from  $0.47$  to  $0.54$   
380 between  $0.2\%$  SS and  $0.4\%$  SS), while in winter,  $\kappa$  decreased with SS (from  $0.50$  to  $0.15$  between  $0.1\%$   
381 SS and  $0.7\%$  SS) (Fig. 3a-b). This contrasting trend may be related to the reduced sulfate fraction in  
382 smaller sizes during winter, as sulfate production via DMS oxidation is diminished due to lower sea  
383 surface temperatures in winter ( $18.0^\circ\text{C}$ ) compared to summer ( $29.3^\circ\text{C}$ ), which in turn inhibits DMS  
384 production by phytoplankton (Bates et al., 1987; Kouvarakis and Mihalopoulos, 2002). Additionally, it  
385 could be linked to the mixing state of the particles, with further discussion provided in the following  
386 sections. The winter  $\kappa$  pattern was similar to observations in the Western North Pacific (Table 1) (Kawana  
387 et al., 2020). Additionally, the winter  $\kappa$  values were comparable to those in Guangzhou (Cai et al., 2020),  
388 adjacent to the SCS, indicating that the northern SCS is influenced by air masses from Mainland China  
389 under the significant influence of the Northeast Monsoon during winter.

### 390 **3.2 Anthropogenic influence on CCN concentration in different seasons**

391 Cluster analysis revealed distinct periods influenced by various air masses. In summer, three  
392 terrestrial air mass sources were identified: Luzon Island (referred to as “Luzon”), Palawan Island, and

393 the Indochinese Peninsula, along with a marine air mass source (Fig. 4a). Given the limited influence of  
394 air masses from Palawan Island, this period was excluded from the study. Consequently, the study  
395 focused on periods dominated by air masses from Luzon (“Luzon” period), the Indochinese Peninsula  
396 (“Indochinese Peninsula” period), and marine sources (“Marine-s” period). In winter, the air mass  
397 sources included Mainland China, a mixture of Mainland China and the South China Sea (referred to as  
398 “Mixed”), and a marine source (Fig. 4b). These were classified as the “Mainland China” period, “Mixed”  
399 period, and “Marine-w” period, respectively.

400 As shown in figure 5, terrestrial air masses could significantly affect the aerosol chemical  
401 composition in the SCS, resulting in higher NR-PM<sub>1</sub> mass concentration and a higher fraction of organic  
402 compounds compared to those influenced by marine air masses. Additionally, the particles number  
403 concentration in the accumulation mode and the N<sub>CCN</sub> at low supersaturation (SS) were higher during  
404 periods influenced by terrestrial air masses (“Luzon” period) than those during marine air mass periods  
405 (Table 2). Notably, we were able to obtain an accurate D<sub>50</sub> at 0.7% supersaturation only during the “Luzon”  
406 period in summer. Due to the relatively lower hygroscopicity compared to other summer periods, the  
407 corresponding D<sub>50</sub> at 0.7% SS ranged between 40 and 60 nm, with relatively high concentration of CN  
408 and CCN (Fig. S7), allowing for a more precise measurement of D<sub>50</sub>. As a result, the  $\kappa$  at 0.7% SS shown  
409 in Fig. 7 was specific to the Luzon period in summer.

410 In summer, the “Luzon” period exhibited the highest N<sub>CN</sub>, attributed to the elevated particle  
411 concentration in the Aitken mode, compared to all other periods in both summer and winter (Fig. 6a and  
412 Table 1). This high fraction of Aitken mode particles led to the lowest bulk AR among the summer  
413 periods (Fig. 7a), as a larger fraction of particles centered on a size range lower than the D<sub>50</sub> (Fig. 7b).  
414 Furthermore, the prevalence of a higher fraction of Aitken mode particles during terrestrial air mass  
415 periods is commonly correlated with the influence of fresh anthropogenic emissions (Beddows et al.,  
416 2015), which could lower the hygroscopicity and consequently suppress the bulk AR.

417 In the “Indochinese Peninsula” period, the N<sub>CN</sub> was lower than it in the “Marine-s” period (Table  
418 2). This difference was mainly due to the variation of Aitken mode particles, while accumulation mode  
419 particles were higher during the “Indochinese Peninsula” period than in “Marine-s” period (Table 2). The  
420 “Marine-s” period primarily occurred during the transition phase before the onset of summer monsoon,  
421 when wind direction shifted from east (Luzon Island direction) to southwest (Indochinese Peninsula  
422 direction). Anthropogenic emissions from Luzon Island still affected the marine atmosphere, leading to

423 higher concentrations of Aitken mode particles compared to the “Indochinese Peninsula” period (Table  
424 2). The higher fraction of accumulation mode particles and higher hygroscopicity during the  
425 “Indochinese Peninsula” period resulted in a higher bulk AR compared to the “Luzon” period. Despite a  
426 higher organic fraction in NR-PM<sub>1</sub> during the “Indochinese Peninsula” period (Fig. 5), hygroscopicity  
427 was still higher due to a higher oxidation degree of organics, indicated by a higher m/z 44 to 43 ratio  
428 (5.87 compared to 5.60 in the “Luzon” period) (Lambe et al., 2011; Jimenez et al., 2009). Additionally,  
429 higher wind speeds during this period (7.26 m s<sup>-1</sup> compared to 3.18 m s<sup>-1</sup> in the “Luzon” period)  
430 potentially led a higher fraction of sea salt (Huang et al., 2022), resulting a higher aerosol hygroscopicity.  
431 Unfortunately, owing to instrument limit, sea salt cannot be detected by the ToF-ACSM.

432 In winter, nitrate accounted for the highest fraction of NR-PM<sub>1</sub> (25.4%) during the “Mainland  
433 China” period compared to other periods (Fig. 5d). Due to similar hygroscopicity between nitrate and  
434 sulfate, as well as comparable inorganic fractions between the “Mainland China” and “Luzon” periods,  
435  $\kappa$  at 0.2% SS was also similar between these two periods (0.30 and 0.33, respectively) (Fig. 7b). However,  
436 aerosol hygroscopicity at small sizes (high SS) was much lower in the “Mainland China” period than in  
437 the “Luzon” period (Fig. 7b), contributing to the low bulk AR in the “Mainland China” period (Fig. 7a).  
438 The BC mass concentration was higher during the “Mainland China” period (2.25  $\mu\text{g m}^{-3}$ ) compared to  
439 the “Luzon” period (0.72  $\mu\text{g m}^{-3}$ ). This suggests that the lower hygroscopicity in smaller particles during  
440 the “Mainland China” period may be attributed to a larger fraction of hydrophobic BC. Additionally, as  
441 discussed in Section 3.1, the reduced biological activity during winter, which results in a decline in the  
442 fraction of small-particle sulfate and an increase in the fraction of organics, may also contribute to this  
443 low hygroscopicity in small particles (at high SS, fig 7b). The similar fractions of Aitken mode and  
444 accumulation particles indicated that PNSD could not fully explain the low bulk AR in the “Mainland  
445 China” period. Overall, lower  $N_{\text{CN}}$  and bulk AR in the “Mainland China” period compared to the “Luzon”  
446 period resulted in a lower  $N_{\text{CCN}}$ .

447 During the “Mixed” period,  $N_{\text{CCN}}$  was lower than in the “Mainland China” period, which can be  
448 attributed to the decreased  $N_{\text{CN}}$  (Table 2). However, accumulation mode particles dominated, unlike in  
449 other terrestrial air mass periods (Fig. 6), resulting in a significantly higher bulk AR compared to the  
450 “Mainland China” period. Organic aerosol hygroscopicity was also higher during the “Mixed” period,  
451 supported by a higher m/z 44 to 43 ratio (3.88 vs. 3.10 in the “Mainland China” period), which explains  
452 the greater hygroscopicity despite a higher organic fraction in NR-PM<sub>1</sub>. Additionally, the lower BC



453 concentration in the “Mixed” period ( $1.20 \mu\text{g m}^{-3}$  vs.  $2.25 \mu\text{g m}^{-3}$  in the “Mainland China” period)  
454 suggests a smaller BC fraction. Moreover, the higher wind speeds during the “Mixed” period ( $10.77 \text{ m}$   
455  $\text{s}^{-1}$  vs.  $7.14 \text{ m s}^{-1}$  in the “Mainland China” period) could have increased the sea salt fraction, further  
456 enhancing aerosol hygroscopicity.

### 457 3.3 CCN closure analysis

458 The CCN closure method is a widely used approach that connects CCN activity with aerosol  
459 chemical composition (Cai et al., 2018; Meng et al., 2014; Deng et al., 2013). Studies have demonstrated  
460 that the aerosol mixing state is crucial for accurately parameterizing CCN activity (Su et al., 2010; Wang  
461 et al., 2010; Ervens et al., 2010). Moreover, the CCN closure method provides a framework for  
462 investigating the influence of aerosol mixing states on CCN activity (Padró et al., 2012; Wang et al.,  
463 2018; Patel et al., 2021). In this study, we applied two schemes based on the CCN closure method, as  
464 described in Section 2.2.3, which consider aerosol composition and mixing state. The fitting parameters  
465 and coefficient of determination ( $R^2$ ) are presented in Table 3, while the fitting plots for both schemes  
466 are shown in Figures S17 and S18. Besides, the NMB from these schemes was presented in Fig. 8.

467 In summer, the NMB was always lower than 0, which indicated that simulated aerosol  
468 hygroscopicity was lower than observed value (Fig. 8). Sea salt which cannot be detected by the ToF-  
469 ACSM may account for higher fraction in summer due to low aerosol concentration in summer (Fig. 3c),  
470 resulting in the underestimation of aerosol hygroscopicity. The NMB exhibits similar trends with changes  
471 in SS in all three periods in summer. Better fitting result appeared at high SS, which indicated a greater  
472 underestimation of the hygroscopicity of larger particles. Besides, “Internal-mixed” scheme had more  
473 precious result than it in “External-mixed” scheme in summer (Fig. 8), suggesting the aerosol was  
474 primary internally mixed in summer.

475 In winter, the “External-mixed” scheme always showed a better result than “Internal-mixed” scheme  
476 at high SS (0.4% SS and 0.7% SS), indicating that particles in small size were mainly externally mixed.  
477 Considering the low hygroscopicity of small-sized particles in winter, it is likely that a significant fraction  
478 of these particles consists of externally mixed BC, which probably originated from fresh anthropogenic  
479 emissions and remains unmixed with other inorganic salts and organics. As BC ages, inorganic and  
480 organic components adhere to it, which would lead to the increase of diameter and particles tended to be  
481 internally mixed (Sarangi et al., 2019). This transition resulted in higher hygroscopicity in large-sized

482 particles compared to the smaller-sized particles. Besides, overestimation of aerosol hygroscopicity at  
483 high SS could be owing to a higher fraction of non- or less- hygroscopic component (such as organic and  
484 BC) at small particle sizes. The predicted  $N_{CCN}$  at 0.1% SS are 20%-40% lower than the observed  
485 concentrations, whereas the predictions at 0.2% SS more closely match the observed values (Fig. 8). This  
486 discrepancy may be due to the higher fraction of sea salt in larger particles. However, due to instrumental  
487 limitations, the ToF-ACSM cannot detect BC and sea salt. Future observations including BC and sea salt  
488 are needed to better assess their effects on aerosol hygroscopicity in the South China Sea (SCS). In  
489 addition, further study of size-resolved aerosol composition can also enhance the understanding on CCN  
490 activity in the SCS.

#### 491 **4. Conclusion**

492 In this study, we investigated the seasonal variations of cloud condensation nuclei (CCN) activity  
493 in the South China Sea (SCS) and explored the impact of anthropogenic emissions. Shipborne  
494 observations were conducted during the summer (May 5–June 9) and winter (December 19–29) of 2021.  
495 We measured CCN activity, chemical composition, and particle number size distribution (PNSD) using  
496 several onboard instruments, including a ToF-ACSM, a CCNc, an SMPS, and an AE33. Observations  
497 included periods before and after the summer monsoon onset and periods influenced by the winter  
498 monsoon.

499 Our results show that particle number concentration ( $N_{CN}$ ) and CCN number concentration ( $N_{CCN}$ )  
500 were higher in summer than in winter, while the mass concentration of non-refractory submicron  
501 particulate matter (NR- $PM_{10}$ ) was lower in summer. This difference is primarily attributed to the  
502 predominance of Aitken mode particles in summer, contrasted with a higher concentration of  
503 accumulation mode particles in winter. Additionally, aerosol hygroscopicity and bulk AR were found to  
504 be higher in summer than in winter.

505 Backward trajectory and cluster analyses identified distinct influences from various air masses. In  
506 summer, we identified periods affected by terrestrial air masses from Luzon Island (the “Luzon” period)  
507 and the Indochinese Peninsula (the “Indochinese Peninsula” period), alongside a period influenced by  
508 marine air masses (the “Marine-s” period). In winter, the periods were influenced by terrestrial air masses  
509 from Mainland China (the “Mainland China” period), a mix of Mainland China and marine sources (the

510 “Mixed” period), and marine air masses (the “Marine-w” period). Terrestrial air mass periods exhibited  
511 higher NR-PM<sub>1</sub> mass concentrations, organic fractions, and N<sub>CCN</sub>, particularly at low supersaturation,  
512 compared to those influenced by marine air masses.

513 During the “Luzon” period, high N<sub>CCN</sub> was observed, attributed to high N<sub>CN</sub>, especially in the Aitken  
514 mode. This high concentration in the Aitken mode resulted in a low bulk AR at 0.2% SS, indicating a  
515 higher fraction of primary organic aerosol with low hygroscopicity. This caused lower overall  
516 hygroscopicity compared to other summer periods. The lower ratio of m/z 44 to 43 also suggested a  
517 lower oxidation degree of organics in this period. In the “Indochinese Peninsula” period, a higher fraction  
518 of the accumulation mode particles compared to the “Luzon” period led to a higher bulk AR, combined  
519 with increased hygroscopicity.

520 In winter, the “Mainland China” period was characterized by a high nitrate fraction in the NR-PM<sub>1</sub>.  
521 The similar inorganic fractions in the NR-PM<sub>1</sub> between the “Mainland China” and “Luzon” periods  
522 resulted in comparable aerosol hygroscopicity at low supersaturation (0.2% SS). However, at higher  
523 supersaturation levels (0.4% and 0.7% SS), the “Mainland China” period demonstrated significantly  
524 lower hygroscopicity, which led to a reduced bulk AR at elevated supersaturation. During the “Mixed”  
525 period, accumulation mode particles predominated, leading to a high bulk AR. This indicated an aging  
526 process during transport, with more oxidized organics and higher aerosol hygroscopicity. The lower black  
527 carbon (BC) fraction and the higher sea salt fraction from high wind speed contributed to higher  
528 hygroscopicity in the “Mixed” period compared to the “Mainland China” period, despite the high organic  
529 fraction.

530 The CCN closure analysis, considering aerosol composition and mixing state, revealed that aerosols  
531 in summer were primarily internally mixed, while in winter, small-sized aerosols were primarily  
532 externally mixed. This distinction is crucial for climate models predicting N<sub>CCN</sub> in the SCS. The  
533 underestimation of aerosol hygroscopicity in summer suggests that the effect of sea salt should be  
534 considered.

535 Our study highlights significant seasonal differences in CCN activity in the SCS and the influence of  
536 different types of terrestrial air masses. Future measurements including size-resolved aerosol  
537 composition and obtain more precise measurements of BC and sea salt are needed to better understanding  
538 CCN activity in this region. Additionally, our observation in winter focused on the CCN activity over the  
539 northern SCS, while the influence of air masses from Mainland China in remote SCS was still unclear.

540 Further observations in remote SCS areas could help clarify the anthropogenic influence during winter  
541 under the effect of the winter monsoon.

542

543 *Data availability.* Data from the measurements are available at [https://doi.org/10.6084/m9.figshare.](https://doi.org/10.6084/m9.figshare.25472545)  
544 [25472545](https://doi.org/10.6084/m9.figshare.25472545) (Ou et al., 2024).

545

546 *Supplement.* The supplement related to this article is available online.

547

548 *Author contributions.* **HO, MC, and JZ** designed the research. **YZ, XN, BL, and CS** performed the  
549 measurements. **HO, MC, QS, and SM** analyzed the data. **SZ and HW** provided useful comments on the  
550 paper. **HO, MC, and JZ** wrote the paper with contributions from all co-authors.

551

552 *Competing interests.* The authors declare that they have no conflict of interest.

553

554 *Financial support.* This work was supported by National Natural Science Foundation of China (NSFC)  
555 (Grant No. 42305123 and 42175115) and Basic and Guangzhou Applied Basic Research Foundation  
556 (Grant No. 2023A1515012240 and 2024A1515030221).

557

558 *Acknowledgements.* Additional support from the crew of the vessels "Tan Kah Kee" and "Sun Yat-sen  
559 University" is greatly acknowledged. We sincerely thank the reviewers and editors for their valuable  
560 suggestions during the review process, which have been instrumental in enhancing the quality of this  
561 manuscript. Lastly, we wish to honor the memory of Professor Zhao Jun and express our heartfelt  
562 gratitude for his significant contributions to this work.

563

564

565 **Reference**

566 Ajith T. C, Kompalli, S. K., and Babu, S. S.: Role of Aerosol Physicochemical Properties on Aerosol  
567 Hygroscopicity and Cloud Condensation Nuclei Activity in a Tropical Coastal Atmosphere, *ACS Earth*  
568 *Space Chem*, 6, 1527-1542, doi:<https://doi.org/10.1021/acsearthspacechem.2c00044>, 2022.

569 Albrecht, B. A.: Aerosols, cloud microphysics, and fractional cloudiness, *Science*, 245, 1227-1230,  
570 doi:<https://doi.org/10.1126/science.245.4923.1227>, 1989.

571 Atwood, S. A., Reid, J. S., Kreidenweis, S. M., Blake, D. R., Jonsson, H. H., Lagrosas, N. D., Xian,  
572 P., Reid, E. A., Sessions, W. R., and Simpas, J. B.: Size-resolved aerosol and cloud condensation nuclei  
573 (CCN) properties in the remote marine South China Sea - Part 1: Observations and source classification,  
574 *Atmos. Chem. Phys.*, 17, 1105-1123, doi:<https://doi.org/10.5194/acp-17-1105-2017>, 2017.

575 Bates, T. S., Cline, J. D., Gammon, R. H., and Kelly-Hansen, S. R.: Regional and seasonal variations  
576 in the flux of oceanic dimethylsulfide to the atmosphere, *J. Geophys. Res. Oceans*, 92, 2930-2938,  
577 doi:<https://doi.org/10.1029/JC092iC03p02930>, 1987.

578 Beddows, D. C. S., Harrison, R. M., Green, D. C., and Fuller, G. W.: Receptor modelling of both  
579 particle composition and size distribution from a background site in London, UK, *Atmos. Chem. Phys.*,  
580 15, 10107-10125, doi:<https://doi.org/10.5194/acp-15-10107-2015>, 2015.

581 Bougiatioti, A., Fountoukis, C., Kalivitis, N., Pandis, S. N., Nenes, A., and Mihalopoulos, N.: Cloud  
582 condensation nuclei measurements in the marine boundary layer of the eastern Mediterranean: CCN  
583 closure and droplet growth kinetics, *Atmos. Chem. Phys.*, 9, 7053-7066, doi:[https://doi.org/10.5194/acp-](https://doi.org/10.5194/acp-9-7053-2009)  
584 [9-7053-2009](https://doi.org/10.5194/acp-9-7053-2009), 2009.

585 Boyer, M., Aliaga, D., Pernov, J. B., Angot, H., Quéléver, L. L. J., Dada, L., Heutte, B., Dall'Osto,  
586 M., Beddows, D. C. S., Brasseur, Z., Beck, I., Bucci, S., Duetsch, M., Stohl, A., Laurila, T., Asmi, E.,  
587 Massling, A., Thomas, D. C., Nøjgaard, J. K., Chan, T., Sharma, S., Tunved, P., Krejci, R., Hansson, H.  
588 C., Bianchi, F., Lehtipalo, K., Wiedensohler, A., Weinhold, K., Kulmala, M., Petäjä, T., Sipilä, M.,  
589 Schmale, J., and Jokinen, T.: A full year of aerosol size distribution data from the central Arctic under an  
590 extreme positive Arctic Oscillation: insights from the Multidisciplinary drifting Observatory for the

591 Study of Arctic Climate (MOSAIC) expedition, *Atmos. Chem. Phys.*, 23, 389-415,  
592 doi:<https://doi.org/10.5194/acp-23-389-2023>, 2023.

593 Burkart, J., Steiner, G., Reischl, G., and Hitzenberger, R.: Long-term study of cloud condensation  
594 nuclei (CCN) activation of the atmospheric aerosol in Vienna, *Atmos Environ*, 45, 5751-5759,  
595 doi:<https://doi.org/10.1016/j.atmosenv.2011.07.022>, 2011.

596 Cai, M., Tan, H., Chan, C. K., Mochida, M., Hatakeyama, S., Kondo, Y., Schurman, M. I., Xu, H.,  
597 Li, F., Shimada, K., Li, L., Deng, Y., Yai, H., Matsuki, A., Qin, Y., and Zhao, J.: Comparison of Aerosol  
598 Hygroscopicity, Volatility, and Chemical Composition between a Suburban Site in the Pearl River Delta  
599 Region and a Marine Site in Okinawa, *Aerosol Air Qual Res*, 17, 3194-3208,  
600 doi:<https://doi.org/10.4209/aaqr.2017.01.0020>, 2017.

601 Cai, M. F., Liang, B. L., Sun, Q. B., Zhou, S. Z., Chen, X. Y., Yuan, B., Shao, M., Tan, H. B., and  
602 Zhao, J.: Effects of continental emissions on cloud condensation nuclei (CCN) activity in the northern  
603 South China Sea during summertime 2018, *Atmos. Chem. Phys.*, 20, 9153-9167,  
604 doi:<https://doi.org/10.5194/acp-20-9153-2020>, 2020.

605 Cai, M. F., Tan, H. B., Chan, C. K., Qin, Y. M., Xu, H. B., Li, F., Schurman, M. I., Liu, L., and Zhao,  
606 J.: The size-resolved cloud condensation nuclei (CCN) activity and its prediction based on aerosol  
607 hygroscopicity and composition in the Pearl Delta River (PRD) region during wintertime 2014, *Atmos.*  
608 *Chem. Phys.*, 18, 16419-16437, doi:<https://doi.org/10.5194/acp-18-16419-2018>, 2018.

609 Chao, Q., Xiao, C., Li, w., Wang, L., Sun, L., Chen, X., Chen, Y., Li, Y., Gao, G., Liu, Y., Zhang,  
610 D., Ai, W., Chen, Y., Cui, T., Dai, T., Feng, A., Guo, Y., Huang, D., Jiang, Y., Li, D., Li, M., Liu, B., Liu,  
611 Y., Lv, Z., Mei, m., Wang, Q., Wang, Y., Yin, Y., Zeng, H., Zhang, Y., Zhai, J., Zhao, L., Zhi, R., Zhong,  
612 H., Zhou, X., Zhou, X., Zhu, X., and Wu, H.: China Climate Bulletin (2022), China Meteorological  
613 Administration, [https://www.cma.gov.cn/zfxxgk/gknr/qxbg/202303/t20230324\\_5396394.html](https://www.cma.gov.cn/zfxxgk/gknr/qxbg/202303/t20230324_5396394.html), 2022.

614 Choi, Y., Rhee, T. S., Collett, J. L., Park, T., Park, S.-M., Seo, B.-K., Park, G., Park, K., and Lee, T.:  
615 Aerosol concentrations and composition in the North Pacific marine boundary layer, *Atmos Environ.*,  
616 171, 165-172, doi:<https://doi.org/10.1016/j.atmosenv.2017.09.047>, 2017.

617       Crosbie, E., Youn, J. S., Balch, B., Wonaschutz, A., Shingler, T., Wang, Z., Conant, W. C., Betterton,  
618 E. A., and Sorooshian, A.: On the competition among aerosol number, size and composition in predicting  
619 CCN variability: a multi-annual field study in an urbanized desert, *Atmos Chem Phys*, 15, 6943-6958,  
620 doi:<https://doi.org/10.5194/acp-15-6943-2015>, 2015.

621       Deng, Z. Z., Zhao, C. S., Ma, N., Ran, L., Zhou, G. Q., Lu, D. R., and Zhou, X. J.: An examination  
622 of parameterizations for the CCN number concentration based on in situ measurements of aerosol  
623 activation properties in the North China Plain, *Atmos. Chem. Phys.*, 13, 6227-6237,  
624 doi:<https://doi.org/10.5194/acp-13-6227-2013>, 2013.

625       Drinovec, L., Močnik, G., Zotter, P., Prévôt, A. S. H., Ruckstuhl, C., Coz, E., Rupakheti, M., Sciare,  
626 J., Müller, T., Wiedensohler, A., and Hansen, A. D. A.: The “dual-spot” Aethalometer: an  
627 improved measurement of aerosol black carbon with real-time loading compensation, *Atmospheric*  
628 *Measurement Techniques*, 8, 1965-1979, doi:<https://doi.org/10.5194/amt-8-1965-2015>, 2015.

629       Dusek, U., Frank, G. P., Hildebrandt, L., Curtius, J., Schneider, J., Walter, S., Chand, D., Drewnick,  
630 F., Hings, S., Jung, D., Borrmann, S., and Andreae, M. O.: Size matters more than chemistry for cloud-  
631 nucleating ability of aerosol particles, *Science*, 312, 1375-1378,  
632 doi:<https://doi.org/10.1126/science.1125261>, 2006.

633       Ervens, B., Cubison, M. J., Andrews, E., Feingold, G., Ogren, J. A., Jimenez, J. L., Quinn, P. K.,  
634 Bates, T. S., Wang, J., Zhang, Q., Coe, H., Flynn, M., and Allan, J. D.: CCN predictions using simplified  
635 assumptions of organic aerosol composition and mixing state: a synthesis from six different locations,  
636 *Atmos. Chem. Phys.*, 10, 4795-4807, doi:<https://doi.org/10.5194/acp-10-4795-2010>, 2010.

637       Fitzgerald, J. W.: Dependence of the Supersaturation Spectrum of CCN on Aerosol Size Distribution  
638 and Composition, *J Atmos Sci*, 30, 628-634, doi:[https://doi.org/10.1175/1520-0469\(1973\)030](https://doi.org/10.1175/1520-0469(1973)030), 1973.

639       Fletcher, Squires, I. b. P., and Bowen, F. b. E. G.: *The Physics of Rainclouds*, 2011.

640       Geng, X. F., Zhong, G. C., Li, J., Cheng, Z. B., Mo, Y. Z., Mao, S. D., Su, T., Jiang, H. Y., Ni, K.  
641 W., and Zhang, G.: Molecular marker study of aerosols in the northern South China Sea: Impact of  
642 atmospheric outflow from the Indo-China Peninsula and South China, *Atmos Environ*, 206, 225-236,  
643 doi:<https://doi.org/10.1016/j.atmosenv.2019.02.033>, 2019.

644 Gras, J. L.: CN, CCN and particle size in Southern Ocean air at Cape Grim, *Atmos Res*, 35, 233-  
645 251, doi:[https://doi.org/10.1016/0169-8095\(94\)00021-5](https://doi.org/10.1016/0169-8095(94)00021-5), 1995.

646 Gras, J. L. and Keywood, M.: Cloud condensation nuclei over the Southern Ocean: wind  
647 dependence and seasonal cycles, *Atmos. Chem. Phys.*, 17, 4419-4432, doi:[https://doi.org/10.5194/acp-](https://doi.org/10.5194/acp-17-4419-2017)  
648 17-4419-2017, 2017.

649 Gysel, M., Crosier, J., Topping, D. O., Whitehead, J. D., Bower, K. N., Cubison, M. J., Williams, P.  
650 I., Flynn, M. J., McFiggans, G. B., and Coe, H.: Closure study between chemical composition and  
651 hygroscopic growth of aerosol particles during TORCH2, *Atmos. Chem. Phys.*, 7, 6131-6144,  
652 doi:<https://doi.org/10.5194/acp-7-6131-2007>, 2007.

653 Heintzenberg, J.: Properties of the Log-Normal Particle Size Distribution, *Aerosol Sci Tech*, 21, 46-  
654 48, doi:<https://doi.org/10.1080/02786829408959695>, 1994.

655 Huang, S., Wu, Z. J., Poulain, L., van Pinxteren, M., Merkel, M., Assmann, D., Herrmann, H., and  
656 Wiedensohler, A.: Source apportionment of the organic aerosol over the Atlantic Ocean from 53 degrees  
657 N to 53 degrees S: significant contributions from marine emissions and long-range transport, *Atmos.*  
658 *Chem. Phys.*, 18, 18043-18062, doi: 10.5194/acp-18-18043-2018, 2018

659 Huang, S., Wu, Z., Wang, Y., Poulain, L., Höpner, F., Merkel, M., Herrmann, H., and Wiedensohler,  
660 A.: Aerosol Hygroscopicity and its Link to Chemical Composition in a Remote Marine Environment  
661 Based on Three Transatlantic Measurements, *Environ. Sci. Technol*, 56, 9613-9622,  
662 doi:<https://doi.org/10.1021/acs.est.2c00785>, 2022.

663 Hussein, T., Dal Maso, M., Petäjä, T., Koponen, I., Paatero, P., Aalto, P., Hämeri, K., and Kulmala,  
664 M.: Evaluation of an automatic algorithm for fitting the particle number size distribution, *Boreal Env.*  
665 *Res*, 10, 337-355, 2005

666 IPCC: Annex I: Observational Products [Trewin, B. (ed.)], in: *Climate Change 2021: The Physical*  
667 *Science Basis. Contribution of Working Group I to the Sixth Assessment Report of the Intergovernmental*  
668 *Panel on Climate Change*, edited by: Masson-Delmotte, V., Zhai, P., Pirani, A., Connors, S. L., Péan, C.,  
669 Berger, S., Caud, N., Chen, Y., Goldfarb, L., Gomis, M. I., Huang, M., Leitzell, K., Lonnoy, E., Matthews,  
670 J. B. R., Maycock, T. K., Waterfield, T., Yelekçi, O., Yu, R., and Zhou, B., Cambridge University Press,



671 Cambridge, United Kingdom and New York, NY, USA, 2061–2086,  
672 <https://doi.org/10.1017/9781009157896.015>, 2021.

673 Jimenez, J. L., Canagaratna, M. R., Donahue, N. M., Prevot, A. S., Zhang, Q., Kroll, J. H., DeCarlo,  
674 P. F., Allan, J. D., Coe, H., Ng, N. L., Aiken, A. C., Docherty, K. S., Ulbrich, I. M., Grieshop, A. P.,  
675 Robinson, A. L., Duplissy, J., Smith, J. D., Wilson, K. R., Lanz, V. A., Hueglin, C., Sun, Y. L., Tian, J.,  
676 Laaksonen, A., Raatikainen, T., Rautiainen, J., Vaattovaara, P., Ehn, M., Kulmala, M., Tomlinson, J. M.,  
677 Collins, D. R., Cubison, M. J., Dunlea, E. J., Huffman, J. A., Onasch, T. B., Alfarra, M. R., Williams, P.  
678 I., Bower, K., Kondo, Y., Schneider, J., Drewnick, F., Borrmann, S., Weimer, S., Demerjian, K., Salcedo,  
679 D., Cottrell, L., Griffin, R., Takami, A., Miyoshi, T., Hatakeyama, S., Shimono, A., Sun, J. Y., Zhang, Y.  
680 M., Dzepina, K., Kimmel, J. R., Sueper, D., Jayne, J. T., Herndon, S. C., Trimborn, A. M., Williams, L.  
681 R., Wood, E. C., Middlebrook, A. M., Kolb, C. E., Baltensperger, U., and Worsnop, D. R.: Evolution of  
682 organic aerosols in the atmosphere, *Science*, 326, 1525-1529,  
683 doi:<https://doi.org/10.1126/science.1180353>, 2009.

684 Kawana, K., Miyazaki, Y., Omori, Y., Tanimoto, H., Kagami, S., Suzuki, K., Yamashita, Y., Nishioka,  
685 J., Deng, Y. G., Yai, H., and Mochida, M.: Number-Size Distribution and CCN Activity of Atmospheric  
686 Aerosols in the Western North Pacific During Spring Pre-Bloom Period: Influences of Terrestrial and  
687 Marine Sources, *J Geophys Res-Atmos*, 127, e2022JD036690,  
688 doi:<https://doi.org/10.1029/2022JD036690>, 2022.

689 Köhler, H.: The nucleus in and the growth of hygroscopic droplets, *Trans. Faraday Soc.*, 32, 1152-  
690 1161, doi:<https://doi.org/10.1039/TF9363201152>, 1936.

691 Kouvarakis, G. and Mihalopoulos, N.: Seasonal variation of dimethylsulfide in the gas phase and  
692 of methanesulfonate and non-sea-salt sulfate in the aerosols phase in the Eastern Mediterranean  
693 atmosphere, *Atmos Environ.*, 36, 929-938, doi:[https://doi.org/10.1016/s1352-2310\(01\)00511-8](https://doi.org/10.1016/s1352-2310(01)00511-8), 2002.

694 Lambe, A. T., Onasch, T. B., Massoli, P., Croasdale, D. R., Wright, J. P., Ahern, A. T., Williams, L.  
695 R., Worsnop, D. R., Brune, W. H., and Davidovits, P.: Laboratory studies of the chemical composition  
696 and cloud condensation nuclei (CCN) activity of secondary organic aerosol (SOA) and oxidized primary  
697 organic aerosol (OPOA), *Atmos. Chem. Phys.*, 11, 8913-8928, doi:[https://doi.org/10.5194/acp-11-8913-](https://doi.org/10.5194/acp-11-8913-2011)  
698 2011, 2011.

699 Latham, T. L. and Nenes, A.: Water Vapor Depletion in the DMT Continuous-Flow CCN Chamber:  
700 Effects on Supersaturation and Droplet Growth, *Aerosol Sci Tech*, 45, 604-615,  
701 doi:<https://doi.org/10.1080/02786826.2010.551146>, 2011.

702 Leena, P. P., Pandithurai, G., Anilkumar, V., Murugavel, P., Sonbawne, S. M., and Dani, K. K.:  
703 Seasonal variability in aerosol, CCN and their relationship observed at a high altitude site in Western  
704 Ghats, *Meteorol Atmos Phys*, 128, 143-153, doi:<https://doi.org/10.1007/s00703-015-0406-0>, 2016.

705 Liang, B., Cai, M., Sun, Q., Zhou, S., and Zhao, J.: Source apportionment of marine atmospheric  
706 aerosols in northern South China Sea during summertime 2018, *Environ. Pollut*, 289, 117948,  
707 doi:<https://doi.org/10.1016/j.envpol.2021.117948>, 2021.

708 Liu, P., Song, M., Zhao, T., Gunthe, S. S., Ham, S., He, Y., Qin, Y. M., Gong, Z., Amorim, J. C.,  
709 Bertram, A. K., and Martin, S. T.: Resolving the mechanisms of hygroscopic growth and cloud  
710 condensation nuclei activity for organic particulate matter, *Nat. Commun*, 9, 4076,  
711 doi:<https://doi.org/10.1038/s41467-018-06622-2>, 2018.

712 Liu, X. and Wang, J.: How important is organic aerosol hygroscopicity to aerosol indirect forcing?,  
713 *Environ. Res. Lett*, 5, 044010, doi:<https://doi.org/10.1088/1748-9326/5/4/044010>, 2010.

714 Liu, Y., Sun, L., Zhou, X., Luo, Y., Huang, W., Yang, C., Wang, Y., and Huang, T.: A 1400-year  
715 terrigenous dust record on a coral island in South China Sea, *Sci Rep*, 4, 4994,  
716 doi:<https://doi.org/10.1038/srep04994>, 2014.

717 Meng, J. W., Yeung, M. C., Li, Y. J., Lee, B. Y. L., and Chan, C. K.: Size-resolved cloud  
718 condensation nuclei (CCN) activity and closure analysis at the HKUST Supersite in Hong Kong, *Atmos.*  
719 *Chem. Phys.*, 14, 10267-10282, doi:<https://doi.org/10.5194/acp-14-10267-2014>, 2014.

720 Miller, R. M., Rauber, R. M., Di Girolamo, L., Rilloraza, M., Fu, D., McFarquhar, G. M., Nesbitt,  
721 S. W., Ziemba, L. D., Woods, S., and Thornhill, K. L.: Influence of natural and anthropogenic aerosols  
722 on cloud base droplet size distributions in clouds over the South China Sea and West Pacific, *Atmos.*  
723 *Chem. Phys.*, 23, 8959-8977, doi:<https://doi.org/10.5194/acp-23-8959-2023>, 2023.

724 Moore, R. H., Nenes, A., and Medina, J.: Scanning Mobility CCN Analysis-A Method for Fast  
725 Measurements of Size-Resolved CCN Distributions and Activation Kinetics, *Aerosol Sci Tech*, 44, 861-  
726 871, doi:<https://doi.org/10.1080/02786826.2010.498715>, 2010.

727 Ou, H., Cai, M., Zhang, Y., Ni, X., Liang, B., Sun, Q., Mai, S., Sun, C., Zhou, S., Wang, H., Sun, j.,  
728 and Zhao, J.: Measurement Report: Seasonal variation and anthropogenic influence on cloud  
729 condensation nuclei (CCN) activity in the South China Sea: Insights from shipborne observations during  
730 summer and winter of 2021 [dataset], doi:<https://doi.org/10.6084/m9.figshare.25472545>, 2024.

731 Ovadnevaite, J., Zuend, A., Laaksonen, A., Sanchez, K. J., Roberts, G., Ceburnis, D., Decesari, S.,  
732 Rinaldi, M., Hodas, N., Facchini, M. C., Seinfeld, J. H., and O' Dowd, C.: Surface tension prevails over  
733 solute effect in organic-influenced cloud droplet activation, *Nature*, 546, 637-641,  
734 doi:<https://doi.org/10.1038/nature22806>, 2017.

735 Padró, L. T., Moore, R. H., Zhang, X., Rastogi, N., Weber, R. J., and Nenes, A.: Mixing state and  
736 compositional effects on CCN activity and droplet growth kinetics of size-resolved CCN in an urban  
737 environment, *Atmos. Chem. Phys.*, 12, 10239-10255, doi:<https://doi.org/10.5194/acp-12-10239-2012>,  
738 2012.

739 Park, M., Yum, S. S., Kim, N., Cha, J. W., Shin, B., and Ryoo, S.-B.: Characterization of submicron  
740 aerosols and CCN over the Yellow Sea measured onboard the Gisang 1 research vessel using the positive  
741 matrix factorization analysis method, *Atmos Res*, 214, 430-441,  
742 doi:<https://doi.org/10.1016/j.atmosres.2018.08.015>, 2018.

743 Patel, P. N. and Jiang, J. H.: Cloud condensation nuclei characteristics at the Southern Great Plains  
744 site: role of particle size distribution and aerosol hygroscopicity, *Environ Res Commun*, 3,  
745 doi:<https://doi.org/10.1088/2515-7620/ac0e0b>, 2021

746 Petters, M. D. and Kreidenweis, S. M.: A single parameter representation of hygroscopic growth  
747 and cloud condensation nucleus activity, *Atmos. Chem. Phys.*, 7, 1961-1971,  
748 doi:<https://doi.org/10.5194/acp-7-1961-2007>, 2007.

749 Pöhlker, M. L., Pöhlker, C., Ditas, F., Klimach, T., Hrabe de Angelis, I., Araújo, A., Brito, J.,  
750 Carbone, S., Cheng, Y., Chi, X., Ditz, R., Gunthe, S. S., Kesselmeier, J., Könemann, T., Lavrič, J. V.,

751 Martin, S. T., Mikhailov, E., Moran-Zuloaga, D., Rose, D., Saturno, J., Su, H., Thalman, R., Walter, D.,  
752 Wang, J., Wolff, S., Barbosa, H. M. J., Artaxo, P., Andreae, M. O., and Pöschl, U.: Long-term  
753 observations of cloud condensation nuclei in the Amazon rain forest – Part 1: Aerosol size distribution,  
754 hygroscopicity, and new model parametrizations for CCN prediction, *Atmos. Chem. Phys.*, 16, 15709-  
755 15740, doi:<https://doi.org/10.5194/acp-16-15709-2016>, 2016.

756 Qin, Y., Wang, H., Wang, Y., Lu, X., Tang, H., Zhang, J., Li, L., and Fan, S.: Wildfires in Southeast  
757 Asia pollute the atmosphere in the northern South China Sea, *Sci Bull (Beijing)*, 69, 1011-1015,  
758 doi:<https://doi.org/10.1016/j.scib.2024.02.026>, 2024.

759 Quinn, P. K., Bates, T. S., Coffman, D. J., and Covert, D. S.: Influence of particle size and chemistry  
760 on the cloud nucleating properties of aerosols, *Atmos. Chem. Phys.*, 8, 1029-1042,  
761 doi:<https://doi.org/10.5194/acp-8-1029-2008>, 2008.

762 Quinn, P. K., Bates, T. S., Coffman, D. J., Upchurch, L., Johnson, J. E., Moore, R., Ziemba, L., Bell,  
763 T. G., Saltzman, E. S., Graff, J., and Behrenfeld, M. J.: Seasonal Variations in Western North Atlantic  
764 Remote Marine Aerosol Properties, *J Geophys Res-Atmos*, 124, 14240-14261,  
765 doi:<https://doi.org/10.1029/2019jd031740>, 2019.

766 Rose, D., Nowak, A., Achtert, P., Wiedensohler, A., Hu, M., Shao, M., Zhang, Y., Andreae, M. O.,  
767 and Pöschl, U.: Cloud condensation nuclei in polluted air and biomass burning smoke near the mega-city  
768 Guangzhou, China - Part 1: Size-resolved measurements and implications for the modeling of aerosol  
769 particle hygroscopicity and CCN activity, *Atmos. Chem. Phys.*, 10, 3365-3383,  
770 doi:<https://doi.org/10.5194/acp-10-3365-2010>, 2010.

771 Ross, K. E., Piketh, S. J., Bruintjes, R. T., Burger, R. P., Swap, R. J., and Annegarn, H. J.: Spatial  
772 and seasonal variations in CCN distribution and the aerosol-CCN relationship over southern Africa, *J*  
773 *Geophys Res-Atmos*, 108, doi:<https://doi.org/10.1029/2002jd002384>, 2003.

774 Safai, P. D., Raju, M. P., Rao, P. S. P., and Pandithurai, G.: Characterization of carbonaceous aerosols  
775 over the urban tropical location and a new approach to evaluate their climatic importance, *Atmos Environ*,  
776 92, 493-500, doi:<https://doi.org/10.1016/j.atmosenv.2014.04.055>, 2014.

777 Sarangi, B., Ramachandran, S., Rajesh, T. A., and Dhaker, V. K.: Black carbon linked aerosol  
778 hygroscopic growth: Size and mixing state are crucial, *Atmos Environ.*, 200, 110-118,  
779 doi:<https://doi.org/https://doi.org/10.1016/j.atmosenv.2018.12.001>, 2019.

780 Schmale, J., Henning, S., Decesari, S., Henzing, B., Keskinen, H., Sellegri, K., Ovadnevaite, J.,  
781 Pohlker, M. L., Brito, J., Bougiatioti, A., Kristensson, A., Kalivitis, N., Stavroulas, I., Carbone, S.,  
782 Jefferson, A., Park, M., Schlag, P., Iwamoto, Y., Aalto, P., Aijala, M., Bukowiecki, N., Ehn, M., Frank,  
783 G., Frohlich, R., Frumau, A., Herrmann, E., Herrmann, H., Holzinger, R., Kos, G., Kulmala, M.,  
784 Mihalopoulos, N., Nenes, A., O'Dowd, C., Petaja, T., Picard, D., Pohlker, C., Poschl, U., Poulain, L.,  
785 Prevot, A. S. H., Swietlicki, E., Andreae, M. O., Artaxo, P., Wiedensohler, A., Ogren, J., Matsuki, A.,  
786 Yum, S. S., Stratmann, F., Baltensperger, U., and Gysel, M.: Long-term cloud condensation nuclei  
787 number concentration, particle number size distribution and chemical composition measurements at  
788 regionally representative observatories, *Atmos. Chem. Phys.*, 18, 2853-2881,  
789 doi:<https://doi.org/10.5194/acp-18-2853-2018>, 2018.

790 Seinfeld, J. H. and Pandis, S. N.: *Atmospheric Chemistry and Physics: From Air Pollution to*  
791 *Climate Change*, Wiley 2016.

792 Sihto, S. L., Mikkilä, J., Vanhanen, J., Ehn, M., Liao, L., Lehtipalo, K., Aalto, P. P., Duplissy, J.,  
793 Petaja, T., Kerminen, V. M., Boy, M., and Kulmala, M.: Seasonal variation of CCN concentrations and  
794 aerosol activation properties in boreal forest, *Atmos. Chem. Phys.*, 11, 13269-13285,  
795 doi:<https://doi.org/10.5194/acp-11-13269-2011>, 2011.

796 Su, H., Rose, D., Cheng, Y. F., Gunthe, S. S., Massling, A., Stock, M., Wiedensohler, A., Andreae,  
797 M. O., and Pöschl, U.: Hygroscopicity distribution concept for measurement data analysis and modeling  
798 of aerosol particle mixing state with regard to hygroscopic growth and CCN activation, *Atmos. Chem.*  
799 *Phys.*, 10, 7489-7503, doi:<https://doi.org/10.5194/acp-10-7489-2010>, 2010.

800 Sun, C., Zhang, Y., Liang, B., Gao, M., Sun, X., Li, F., Ni, X., Sun, Q., Ou, H., Chen, D., Zhou, S.,  
801 and Zhao, J.: Morphological and optical properties of carbonaceous aerosol particles from ship emissions  
802 and biomass burning during a summer cruise measurement in the South China Sea, *Atmos. Chem. Phys.*,  
803 24, 3043-3063, doi:<https://doi.org/10.5194/acp-24-3043-2024>, 2024.

804 Sun, Q., Liang, B., Cai, M., Zhang, Y., Ou, H., Ni, X., Sun, X., Han, B., Deng, X., Zhou, S., and  
805 Zhao, J.: Cruise observation of the marine atmosphere and ship emissions in South China Sea: Aerosol  
806 composition, sources, and the aging process, *Environ. Pollut.*, 316, 120539,  
807 doi:<https://doi.org/10.1016/j.envpol.2022.120539>, 2023.

808 Wang, B., Huang, F., Wu, Z., Yang, J., Fu, X., and Kikuchi, K.: Multi-scale climate variability of  
809 the South China Sea monsoon: A review, *Dynam Atmos Oceans*, 47, 15-37,  
810 doi:<https://doi.org/10.1016/j.dynatmoce.2008.09.004>, 2009. Wang, Y., Chen, J., Wang, Q., Qin, Q., Ye, J.,  
811 Han, Y., Li, L., Zhen, W., Zhi, Q., Zhang, Y., and Cao, J.: Increased secondary aerosol contribution and  
812 possible processing on polluted winter days in China, *Environ Int*, 127, 78-84,  
813 doi:<https://doi.org/10.1016/j.envint.2019.03.021>, 2019.

814 Wang, J., Cubison, M. J., Aiken, A. C., Jimenez, J. L., and Collins, D. R.: The importance of aerosol  
815 mixing state and size-resolved composition on CCN concentration and the variation of the importance  
816 with atmospheric aging of aerosols, *Atmos. Chem. Phys.*, 10, 7267-7283,  
817 doi:<https://doi.org/10.5194/acp-10-7267-2010>, 2010.

818 Wang, Q., and Sun, Y.: Characterization of aerosol hygroscopicity, mixing state, and CCN activity  
819 at a suburban site in the central North China Plain, *Atmos. Chem. Phys.*, 18, 11739-11752,  
820 doi:<https://doi.org/10.5194/acp-18-11739-2018>, 2018.

821 Wang, Y. Q.: MeteoInfo: GIS software for meteorological data visualization and analysis, *Meteorol.*  
822 *Appl*, 21, 360-368, doi:<https://doi.org/10.1002/met.1345>, 2014.

823 Xiao, H.-W., Xiao, H.-Y., Luo, L., Shen, C.-Y., Long, A.-M., Chen, L., Long, Z.-H., and Li, D.-N.:  
824 Atmospheric aerosol compositions over the South China Sea: temporal variability and source  
825 apportionment, *Atmos. Chem. Phys.*, 17, 3199-3214, doi:<https://doi.org/10.5194/acp-17-3199-2017>,  
826 2017.

827 Zheng, G., Kuang, C., Uin, J., Watson, T., and Wang, J.: Large contribution of organics to  
828 condensational growth and formation of cloud condensation nuclei (CCN) in the remote marine boundary  
829 layer, *Atmos. Chem. Phys.*, 20, 12515-12525, doi:<https://doi.org/10.5194/acp-20-12515-2020>, 2020.

830       Zhu, K. and Wang, L.: A comprehensive study on the validation and application of multi-lognormal  
831 distribution models for atmospheric particles, *Atmos Environ.*, 338, 120813,  
832 doi:<https://doi.org/10.1016/j.atmosenv.2024.120813>, 2024.

833

834 Table 1. The number concentration of particle and cloud condensation nuclei at different supersaturation (SS), the hygroscopicity and bulk activation ratio (AR), and activation  
835 diameter ( $D_{50}$ ) at different SS in different studies.



Deleted:

Location	period	$N_{CN}$ (cm <sup>-3</sup> )	$N_{CCN}$ (cm <sup>-3</sup> )	Hygroscopicity ( $\kappa$ )	Bulk AR	$D_{50}$ (nm)	Reference
South China Sea	2021.05.05-	6966±9249	2640±3639 (0.20% SS)	0.47±0.21 (0.20% SS)	0.37±0.16 (0.20% SS)	96±19 (0.20% SS)	This study
	2021.06.09		4392±6415 (0.40% SS)	0.54±0.21 (0.40% SS)	0.63±0.17 (0.40% SS)	57±9 (0.40% SS)	
Northern South China Sea	2021.12.19-	4988±3474	1086±691 (0.10% SS)	0.50±0.21 (0.10% SS)	0.23±0.09 (0.10% SS)	145±18 (0.10% SS)	This study
	2021.12.29		1625±1110 (0.20% SS)	0.31±0.10 (0.20% SS)	0.33±0.12 (0.20% SS)	107±13 (0.20% SS)	
			2218±1503 (0.40% SS)	0.19±0.05 (0.40% SS)	0.44±0.13 (0.40% SS)	79±7 (0.40% SS)	
Northern South China Sea	2018.08.06-	3463	1544 (0.34% SS)	0.38±0.09 (0.18% SS)	/	/	Cai et al., 2020
	2018.08.27			0.38±0.08 (0.59% SS)			
Remote South China Sea	2012.09.14-	503±455	450±388 (0.14% SS)	0.54±0.14 (0.14% SS)	0.47±0.16 (0.14% SS)	/	Atwood et al., 2017
	2012.09.26		675±516 (0.38% SS)	0.50±0.21 (0.38% SS)	0.72±0.17 (0.38% SS)		
			698±555 (0.53% SS)	0.50±0.21 (0.38% SS)	0.79±0.15 (0.53% SS)		
Western North Pacific	2015.03.04-	/	/	0.75±0.21 (0.11% SS)	0.40±0.22 (0.11% SS)	/	Kawana et al., 2020
	2015.03.26			0.51±0.16 (0.24% SS)	0.50±0.22 (0.24% SS)		
				0.45±0.16 (0.60% SS)	0.70±0.23 (0.60% SS)		
Guangzhou	2014.11-	/	3103±1913 (0.10% SS)	0.37±0.11 (0.10% SS)	0.26±0.10 (0.10% SS)	156 ± 19 (0.1% SS)	Cai et al., 2018
	2014.12		5095±2972 (0.20% SS)	0.29±0.09 (0.20% SS)	0.41±0.14 (0.20% SS)	107 ± 17 (0.2% SS)	
			6524±3783 (0.40% SS)	0.18±0.07 (0.40% SS)	0.53±0.15 (0.40% SS)	78 ± 15 (0.4% SS)	
Yellow Sea	2017.04-	7622±4038	7913±4234 (0.70% SS)	0.15±0.06 (0.70% SS)	0.64±0.13 (0.70% SS)	58 ± 11 (0.7% SS)	Park et al., 2018
	2017.05		4821±1763 (0.63% SS)	/	/	/	

838 Table 1. The number concentration of particle and cloud condensation nuclei at different supersaturation (SS), the hygroscopicity and bulk activation ratio (AR), and activation  
839 diameter ( $D_{50}$ ) at different SS in different studies.

Cluster	Summer			Winter		
	Indochinese Peninsula	Luzon	Marine	Mainland China	Marine	Mixed
$N_{CCN}$ ( $cm^{-3}$ )						
0.1% SS	\	\	\	1359±669	439±223	945±400
0.2% SS	1200±787	4066±4748	1135±800	2058±1095	614±318	1460±514
0.4% SS	1650±1187	7804±8608	1812±1052	2792±1478	830±424	1801±640
0.7% SS	2239±1367	10480±9741	2515±1523	3514±1841	1024±463	2101±757
$N_{CN}$ ( $cm^{-3}$ )						
Total	2699±2147	14674±13844	3033±2366	6875±3263	1728±465	2918±1204
Nucleation	111±206	1543±3341	238±426	893±925	214±281	141±191
Aikten	1156±1261	8653±8815	1668±1526	3089±2017	732±337	806±427
Accumulation	1434±1444	3764±4157	1121±929	2923±2440	781±313	1975±831
Bulk AR						
0.1% SS	\	\	\	0.21±0.07	0.26±0.10	0.32±0.04
0.2% SS	0.49±0.13	0.31±0.17	0.40±0.13	0.30±0.09	0.36±0.14	0.51±0.05
0.4% SS	0.73±0.09	0.55±0.18	0.68±0.14	0.40±0.10	0.49±0.16	0.63±0.06
0.7% SS	0.98±0.15	0.76±0.16	0.90±0.13	0.50±0.09	0.61±0.18	0.73±0.06

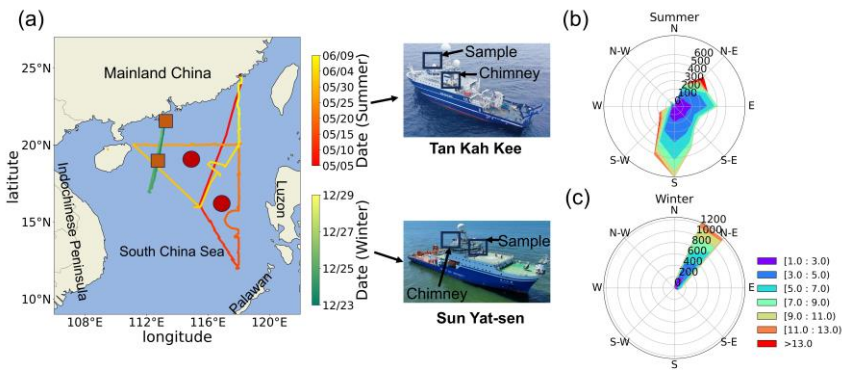
841 Table 2. The number concentration of particle, cloud condensation nuclei, and bulk activation ratio in  
842 different periods.

Cluster	Summer			Winter		
	Luzon	Indochinese Peninsula	Marine	Mainland China	Mixed	Marine
<b>Internal scheme</b>						
0.1% SS	\	\	\	0.91 (0.97)	0.72 (0.95)	0.71 (0.94)
0.2% SS	0.83 (0.89)	0.89 (0.81)	0.76 (0.96)	1.13 (0.96)	1.01 (0.99)	0.94 (0.97)
0.4% SS	0.90 (0.96)	0.90 (0.98)	0.89 (0.97)	1.34 (0.97)	1.14 (0.98)	1.04 (0.98)
0.7% SS	0.91 (0.93)	0.96 (0.92)	0.88 (0.98)	1.38 (0.97)	1.16 (0.99)	1.04 (0.96)
<b>External scheme</b>						
0.1% SS	\	\	\	0.80 (0.97)	0.62 (0.95)	0.59 (0.94)
0.2% SS	0.74 (0.88)	0.77 (0.79)	0.80 (0.96)	1.01 (0.97)	0.90 (0.99)	0.81 (0.97)
0.4% SS	0.78 (0.93)	0.80 (0.97)	0.82 (0.96)	1.23 (0.97)	1.05 (0.98)	0.95 (0.98)
0.7% SS	0.80 (0.92)	0.89 (0.92)	0.80 (0.98)	1.24 (0.98)	1.11 (0.99)	1.00 (0.96)

845 Table 3. The slope and coefficient of determination (in parentheses) in CCN closure analysis at  
846 different supersaturations in different periods.

847

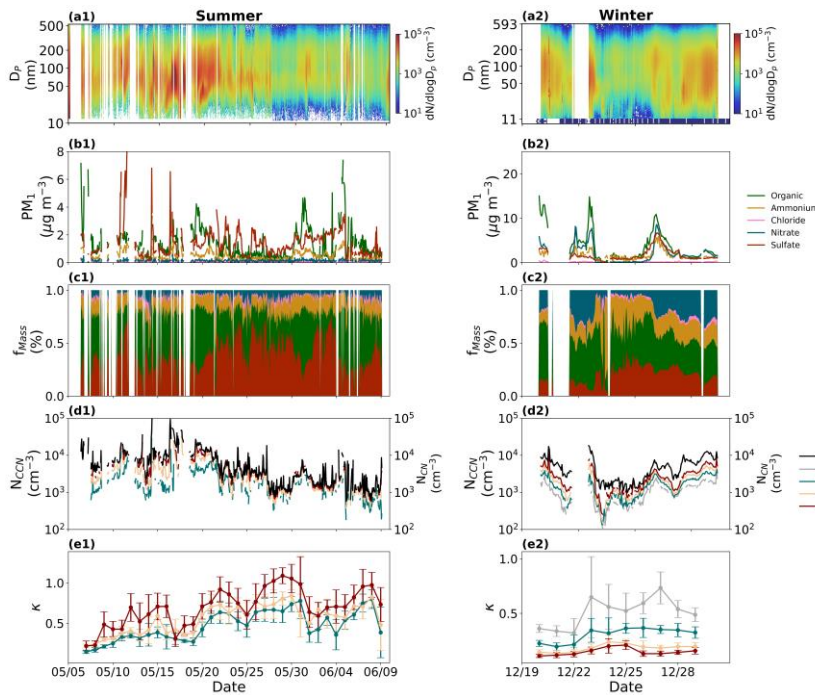
848



849

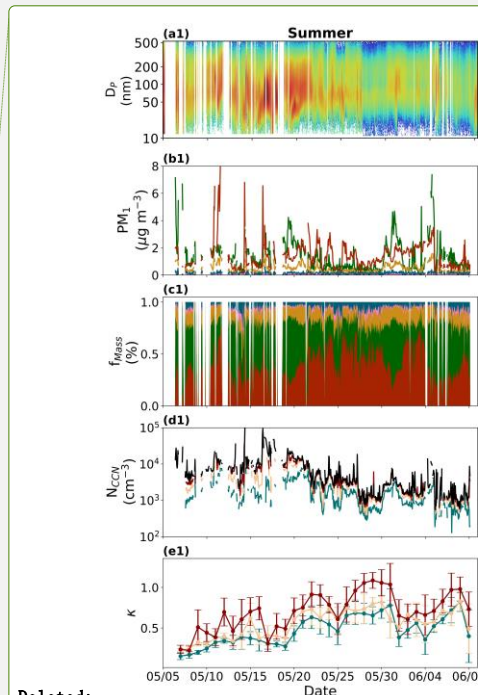
850 Figure 1. The cruises of two shipborne observations, and the location of sample line and chimney of Tan  
851 Kah Kee, and Sun Yat-sen scientific vessel (a); Wind rose of the wind direction and wind speed in  
852 summer and winter cruises; The radius represents the frequency of wind direction occurrences, and the  
853 shaded areas indicate wind speed (b) and (c). The red circles are the midpoints of the ship trajectory  
854 selected for backward trajectory and cluster analysis in summer and the orange squares are the midpoints  
855 of the ship trajectory selected for backward trajectory and cluster analysis in winter.

Formatted: Justified



857

858 Figure 2. Timeseries of (a) particle number size distribution, (b) mass concentration of NR-PM1, and (c)  
 859 its fraction, (d) number concentration of total particle and cloud condensation nuclei under the  
 860 supersaturation of 0.1%, 0.2%, 0.4%, and 0.7%, and (e) aerosol hygroscopicity. The number 1 in figure  
 861 number means timeseries in summer and number 2 means it in winter.



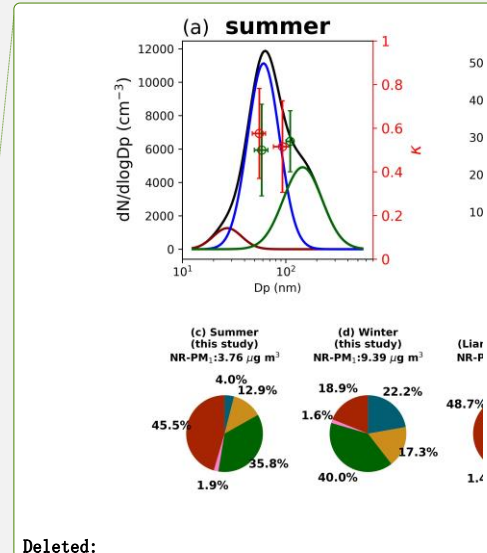
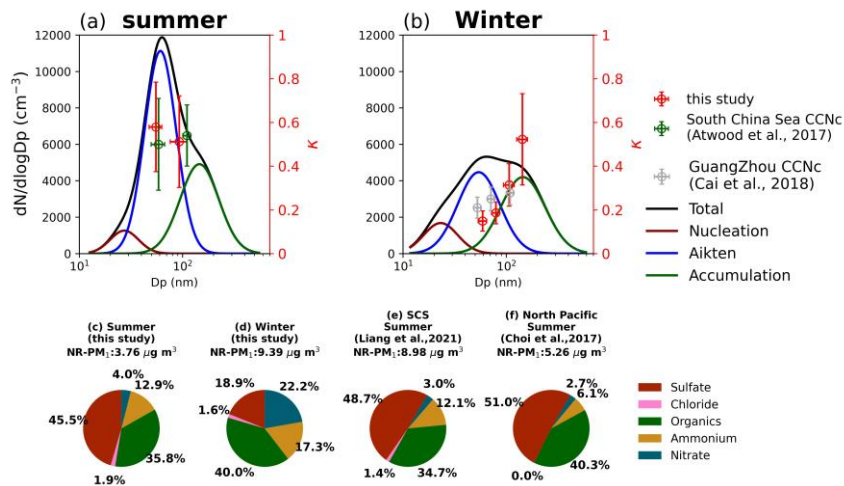
Deleted:

Formatted: Justified

Deleted: (d) mass concentration of organic carbon and elemental carbon,

Deleted: e

Deleted: f



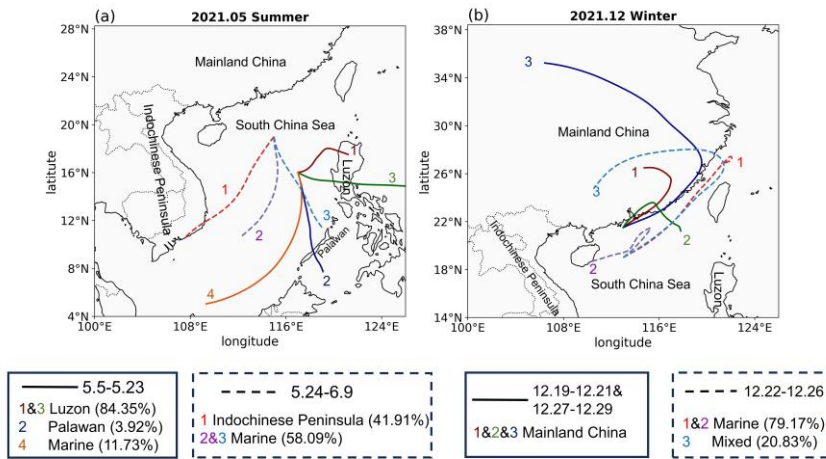
867

868 Figure 3. Particle number size distribution in summer (a) and winter (b); The red markers represent the  
 869 activation diameters and hygroscopicity parameters corresponding to 0.1%, 0.2%, 0.4%, and 0.7%  
 870 supersaturations in this study (without 0.1% in summer). The green markers represent the hygroscopicity  
 871 parameters reported in Atwood et al. (2017) for the southern South China Sea during summer. The gray  
 872 markers represent the hygroscopicity parameters documented in Cai et al. (2018) for the Pearl River  
 873 Delta region during winter. The fraction of NR-PM<sub>1</sub> in summer (c) and winter (d) in this study, in northern  
 874 SCS reported by Liang et al. (2021) (e), and in North Pacific reported by Choi et al. (2017) (f).

Deleted:

Formatted: Justified

Deleted:



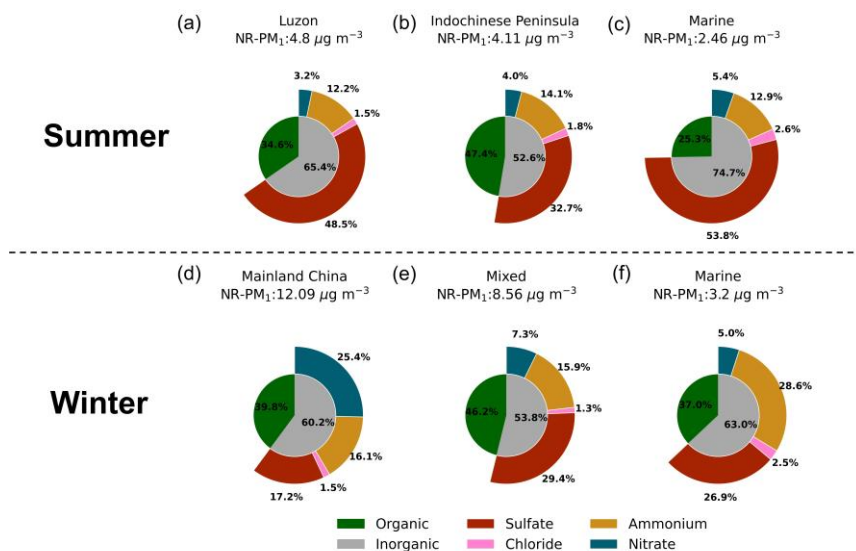
877

878 Figure 4. The cluster analysis results in summer (a) and winter (b). The solid line in summer means  
 879 cluster analysis from May 5 to May 24 and the dash line in summer means cluster analysis from May 25  
 880 to June 9; The solid line in winter means cluster analysis from Dec 19 to Dec 21 and Dec 27 to Dec 29,  
 881 and the dash line in winter means cluster analysis from Dec 22 to Dec 26.

Formatted: Justified



882



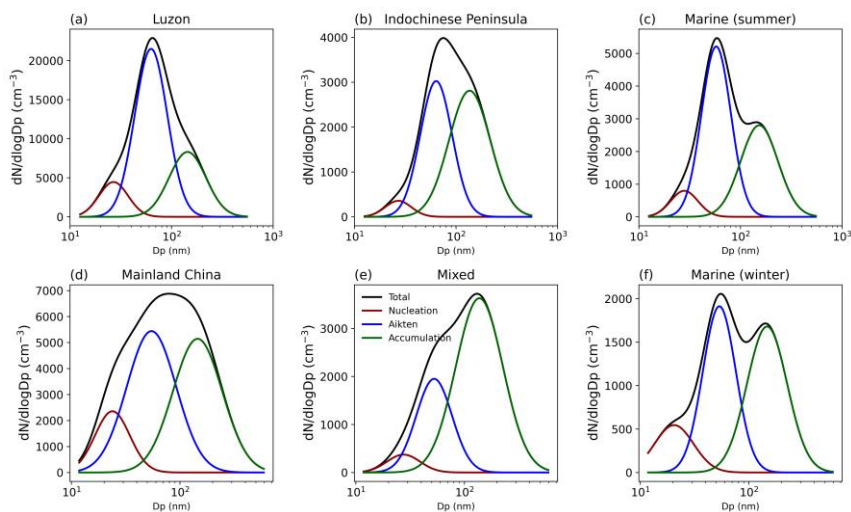
883

884 Figure 5. The fraction of NR-PM<sub>1</sub> in “Luzon” period (a), “Indochinese Peninsula” period (b), and  
885 “Marine-s” period (c) in summer. The fraction of NR-PM<sub>1</sub> in “Mainland China” period (d), “Mixed”  
886 period (e), and “Marine-w” period (f) in winter.

Formatted: Justified

Formatted: Subscript

887



888

889

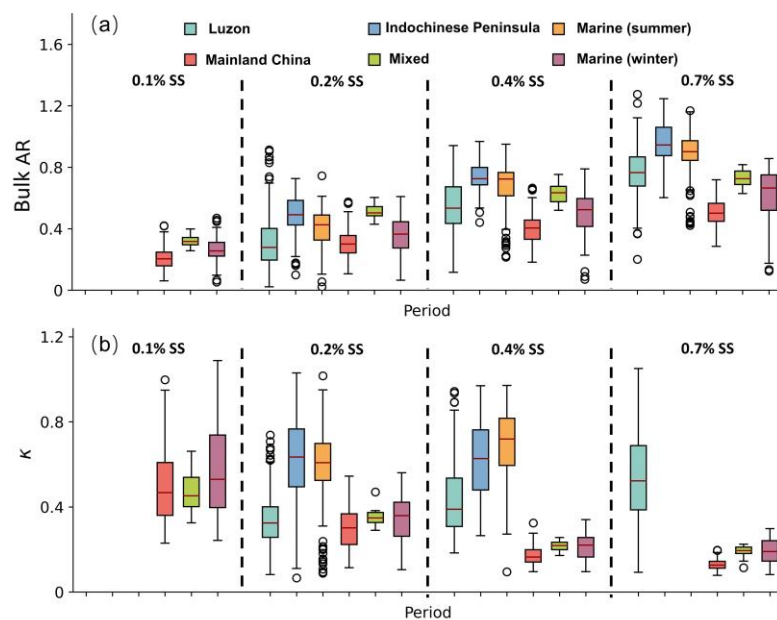
890

891

Figure 6. The particle number size distribution (PNSD) in “Luzon” period (a), “Indochinese Peninsula” period (b), and “Marine-s” period (c) in summer. The PNSD in “Mainland China” period (d), “Mixed” period (e), and “Marine-w” period (f) in winter.

Formatted: Justified

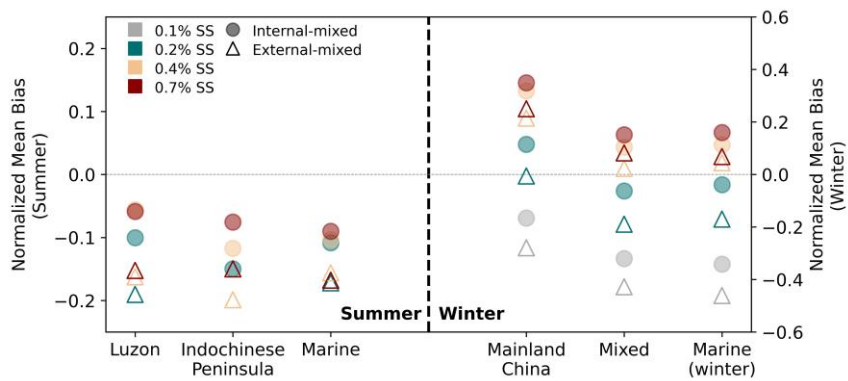
892



893

894 Figure 7. The bulk activation ratio (AR) at different supersaturation (SS) in different periods (a); The  
895 aerosol hygroscopicity ( $\kappa$ ) at different supersaturation (SS) in different periods (b).

Formatted: Justified



896

897

898

899

900

Figure 8. The normalized mean bias (NMB) calculated by “Internal-mixed” scheme and “External-mixed” scheme according to CCN closure method. The marker of circle means “Internal-mixed” scheme and the marker of triangle means “External-mixed” scheme. Different colors mean different supersaturations.

Formatted: Justified

Deleted: means